Measurement and Analysis of Wavefront Deviations and Distortions by Freeform Optical See-through Head Mounted Displays

by

Jason Kuhn

A Master's Thesis Submitted to the Faculty of the

COLLEGE OF OPTICAL SCIENCES

In Partial Fulfillment of the Requirements

For the Degree of

MASTER OF SCIENCE

In the Graduate College

THE UNIVERSITY OF ARIZONA

2016

STATEMENT BY AUTHOR

This thesis has been submitted in partial fulfillment of the requirements for an advanced degree at the University of Arizona and is deposited in the University Library to be made available to borrowers under rules of the Library.

Brief quotations from this thesis are allowable without special permission, provided that an accurate acknowledgement of the source is made. Requests for permission for extended quotation from or reproduction of this manuscript in whole or in part may be granted by the head of the major department or the Dean of the Graduate College when in his or her judgment the proposed use of the material is in the interests of scholarship. In all other instances, however, permission must be obtained from the author.

SIGNED:_____
Jason Kuhn

APPROVAL BY THESIS DIRECTOR

This thesis has been approved on the date shown below:

_____ _____
Hong Hua Date
Professor of Optical Sciences

ACKNOWLEDGEMENTS

I want to give many thanks to my academic advisor, Dr. Hong Hua. Throughout my academic career, she was more than an advisor to me, she was also a role model and a friend. I also want express my appreciation to my colleagues in the 3DVIS Lab. Dewen Cheng for his patience with teaching me Code V back in 2010. Xinda Hu was always there to help whenever I needed it, even after he graduated. Yi Qin, Sheng Huei Lu, and Sangyoon Lee were also invaluable lab mates whether it was trying to find a lost lenslet array in the lab or fixing a bug in my MATLAB code. J.J. Katz was a huge help with my Hartmann testing. I also want to acknowledge the OSC faculty and staff, specifically Cindy Gardner, Amanda Ferraris, and Mark Rodriguez. They were always so friendly and helped me in so many ways that I am very grateful for everything they did for me.

DEDICATION

To my parents, Mark and Cindy and my girlfriend, Jessica. I could not have done it without your love and support.

TABLE OF CONTENTS

TABLE OF FIGURES

Abstract

A head-mounted-display with an optical combiner may introduce significant amount of distortion to the real world scene. The ability to accurately model the effects of both 2-dimensional and 3-dimensional distortion introduced by thick optical elements has many uses in the development of head-mounted display systems and applications. For instance, the computer rendering system must be able to accurately model this distortion and provide accurate compensation in the virtual path in order to provide a seamless overlay between the virtual and real world scenes. In this paper, we present a ray tracing method that determines the ray shifts and deviations introduced by a thick optical element giving us the ability to generate correct computation models for rendering a virtual object in 3D space with the appropriate amount of distortion.

We also demonstrate how a Hartmann wavefront sensor approach can be used to evaluate the manufacturing errors in a freeform optical element to better predict wavefront distortion. A classic Hartmann mask is used as an inexpensive and easily manufacturable solution for accurate wavefront measurements. This paper further suggests two techniques; by scanning the Hartmann mask laterally to obtain dense sampling and by increasing the view screen distance to the testing aperture, for improving the slope measurement accuracy and resolution. The paper quantifies the improvements of these techniques on measuring both the high and low sloped wavefronts often seen in freeform optical-see-through head-mounted displays. By comparing the measured wavefront to theoretical wavefronts constructed with ray tracing software, we determine the sources of error within the freeform prism. We also present a testing setup capable of

measuring off-axis viewing angles to replicate how the system would perform when worn by its user.

1: Introduction

A see-through display is a key enabling technology to an augmented reality (AR) system that combines a computer-generated virtual image with the physical objects seen in real world scenes. There are two different approaches to a see-through AR display: video-see-through and optical-see-through. A video see-through AR display uses a camera system to capture the view of the real world and digitally combines the image with the computer-generated virtual world. This approach makes it easy to combine the real and virtual scenes but there is inevitable degradation to the real world viewing experience. An optical see-through AR display optically combines the virtual scene directly to the real world scene through an optical combiner (e.g. a beamsplitter) which imposes minimal optical degradation to the real world scene. The optical-see-through head-mounted-display (OST HMD) is the focus of this paper.

Over the past few decades, many different optical design approaches have been applied to HMD eyepiece designs to improve the system performance. Optical combiner technology has significant influence on the performance and form factor of an OST-HMD. The simplest and most common type of optical combiner is a plane parallel plate (PPP) with a flat beamsplitting surface [1]. The plate may be tilted by an angle (e.g. horizontally or vertically at 45-degrees) to fold the optical path of the virtual display while maintaining a direct view of the real world. Another type is a waveguide solid in which the entire combiner remains relatively parallel (or at a small angle) to the direction of the interpupillary separation, and a beamsplitting surface is embedded inside the combiner element. The viewer directly sees the real world view through the entire

combiner element. For instance, the well-advertised Google Glass [2], shown below in Figure 1, is a very compact, lightweight (~36grams), monocular OST-HMD. It uses a solid waveguide combiner. Another similar example is the Epson Moverio [3].

Figure 1. Google Glass, a commercially available OST HMD [2]

Another different combiner used in OST HMD design available to consumers is made by Lumus [4]. One of their newer designs is shown below in Figure 2 (top). They use a patented waveguide technology with an array of engineered micro-beamsplitters embedded within the glass substrate to redirect different field angles to the viewer, this is shown in Figure 2 (bottom).

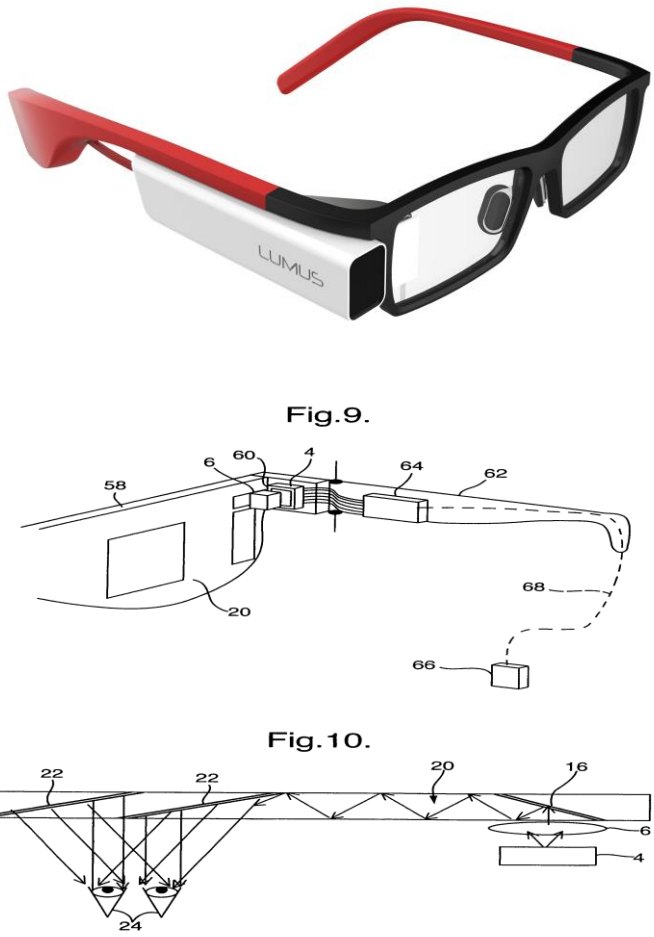

Figure 2. Lumus's patented waveguide OST HMD showing how different field angles are reflected by unique beamsplitters [4]

This allows for a very compact and thin combiner design, similar to what would be worn in your typical eyeglasses. However, there are problems with ghost imaging that affects the image quality. The mirrors, labeled with the #22 in the patent drawing seen in Figure 2 (bottom), have a highly tuned angular dependent reflection coefficient. The field angle is maintained as light travels through the waveguide. The desired angular range will be mostly reflected by one mirror, however these mirrors are not perfect filters and some

light from the wrong field angles will be reflected causing a ghost image or haze in the virtual image.

Holographic optical element (HOE) is another technology used for optical combiner in OST-HMDs. Sony released the developer kit for the SmartEyeGlass in Spring of 2015 which utilizes this technology [5]. It features a monochrome green display with a 20° diagonal field of view and a 419x138 resolution. The advantages to this design are a lightweight (77grams) form factor with only a 3mm lens thickness and a 85% lens transmission making it comfortable to wear.

Figure 3: SONY SmartEyeGlass OST-HMD design featuring an HOE lens [5]

Figure 4 shows another type of solid waveguide combiners using a wedge-shaped freeform eyepiece [7]. This layout shows the real world image being combined with the virtual image of the microdisplay with both images being presented to user's eye. The see-through eyepiece consists of two cemented components, a wedge-shaped freeform prism and wedge-shaped freeform compensation lens. The user's eye is placed at the exit

pupil of the system, typically with an eye relief of 15-25mm. Surface 2 is a freeform surface with a beamsplitting coating, which facilitates the combiner function. This layout shows the real world image being combined with the virtual image of the microdisplay with both images being presented to user's eye.

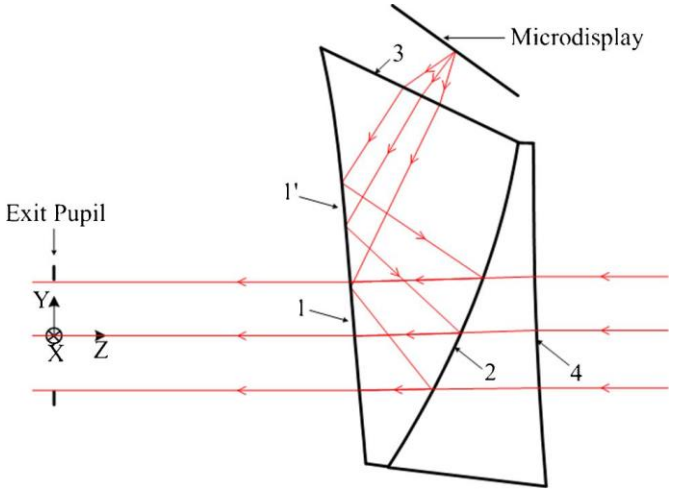

Figure 4. The layout of an optical combiner showing the real world path passing through surfaces 2 and 4 and the virtual path reflected off of 2 and 1' and passing through surface 3 [7]

In OST-HMDs, the light rays generated from microdisplays of HMDs are merged with those from a physical scene through the different types of optical combiners of finite thickness. The light rays from the real world typically follow a refractive path through the combiner and are deviated from their incident directions before reaching the eyes. As a result, the apparent distance, position, and even the shape of the real objects may be shifted or distorted. The type and amount of optical distortion to the physical worlds depend on many factors, including the shape, thickness, and orientation of the combiner element. The thicker the optical combiner, the larger the effective ray deviation. The magnitude of this effect also depends on the angle of the combiner with respect to the

viewing axis. For instance, more than 1 pixel change in binocular image disparity may be caused for viewing physical objects at arm-length through a flat beamsplitter of 1 mm thickness with a refractive index of 1.5, angled at 45 degrees with respect to the viewing axis, [6]. This type of perception distortion to the real-world view due to combiner becomes an even more significant factor in systems using a thick combiner. For instance, the combiner thickness for both the popular Google glass and the Epson Moverio displays are approximately 10 mm, while the thickness of the emerging OST-HMDs using freeform wedge-shaped prisms along with a see-through compensator lens can be even greater, typically between 10-25mm depending on the system field of view and other display parameters [7]. The complex freeform surface shapes used in the freeform waveguide solids are expected to cause much more complex wavefront distortion to the see-through view than a flat surface combiner.

In many applications it is advantageous to seamlessly overlay the virtual image over the real world view. For example a surgeon looking at a human torso with virtual X-ray imaging information displayed by an OST-HMD would need the X-ray image to appear in the correct 3-D space to maximize its effectiveness. Applications such as this make it desirable for the 3D distortion seen in the real world view of an OST HMD to be accurately simulated and quantified.

The main contributions of this thesis are two folds. The first contribution is the development of a ray tracing method to predict the depth distortion caused by an optical combiner. We simulate different geometries typically seen in AR systems and summarize the effects of combiner thickness, IPD, system combiner orientation, viewing angle, and object distance on the see-through distortion. This ray tracing method

described in this paper is also capable of simulating the depth distortion introduced by complex surface shapes. The ray tracing algorithm described in allows us to estimate the ray deviations leading to convergence errors for the viewer. The second contribution is the development of a Hartman Wavefront sensor method for accurately measuring the distorted wavefront caused by a freeform waveguide combiner for OST-HMDs.

The rest of the thesis is organized as follows. Chapter 2 overviews related work, Chapter 3 presents the ray tracing method for the depth distortion simulation and results, and Chapter 4 describes the setup, procedure and results of the Hartmann wavefront testing method for freeform wavefront measurement.

2. Background and Related Work

2.1 Depth Distortion

Various studies have investigated the possible error sources leading to depth perception errors in AR. Some examples of these error sources include improper display calibration [8] mismatch between accommodation and convergence caused by the ray-shift phenomenon [9], interpupillary distance variation (IPD) [6], and the finite image resolution of the virtual display [10].

Most of these studies have been user perception studies where the test subject has to estimate the depth of the virtual object. There are different proposed methods for these tests, but it has been demonstrated that the most accurate tests are the perceptual matching tests, where the test subject is presented with a virtual and real object and are instructed to adjust the distance of one of those objects until the perceived depth matches as closely as possible. This testing method has proven to be more accurate than the

methods of constant stimuli, blind walking test, and blind reach tests. However, the perceptual matching studies generally have found that measured depth is underestimated by the test subjects.

Lee and Hua et al [6] investigated the ray-shift phenomenon and IPD variation as an error source of the incorrect depth perception with regards to convergence. After proposing a method for correction for these depth perception errors they were able to demonstrate significant correction (less than 1% residual error) to the depth perception errors introduced by an AR system with a user based study examining near-field convergence. Their method for compensating for the depth perception error uses a similar ray tracing approach as the one discussed in this paper but they only examine simple AR geometries and they do not investigate the effects of accommodation on the perception error caused by OST-HMDs.

Itoh and Klinker [11] proposed a light field-based technique to correct registration errors between the virtual and real world scenes in OST-HMDs. They determined that the difference in refraction of the virtual and physical ray paths induced by the OST-HMDs can cause depth estimation errors but they have not yet investigated how this correlates to perceptual issues as seen by the user. Hoffman and Gishick et al [12] demonstrate how the mismatch between accommodation and convergence commonly seen in 3D displays will cause visual fatigue and hinder visual performance. They are able to closely match these visual cues in their 3D display and employ a user study to show an improvement in the visual performance of their test subjects. They do not investigate what specific AR parameters causes these registration errors.

In this paper, we further examine the effects of the ray-shift phenomenon caused by an optical combiner on depth perception in both monocular and binocular geometries. We examine the effects of IPD, tilt, FOV, element thickness, object distance, and complex surface shapes and a present a summary of how these parameters affect the depth perception seen in OST HMDs.

2.2 Freeform Wavefront Testing

The theoretical depth distortion modelling of OST HMDs presented in this paper is limited by the precision in the manufacturing of these complex prism shapes. Most high accuracy surface testing today is performed with interferometry, however with freeform OST HMD prisms the surface shape is too curved to be tested with typical interferometric approaches. A null-interferometer using a custom wavefront via a computer generated hologram matching the known theoretical shape of your design [13] is a possible solution, but this approach is expensive and a new CGH must be made for each design. This isn't always practical when testing a single part or prototype. Fringe projection techniques use structured illumination [14]. A sinusoidal fringe pattern is projected on your test piece and a camera examines spatial shifts in the pattern to accurately triangulate the test piece coordinates in 3D space. Unfortunately this method requires non-specular surfaces and can't be used with our OST HMD prisms. Fringe reflection techniques avoid this problem by projecting the structured image directly onto the camera sensor after reflecting off the specular test surface [15]. Small changes in surface slope cause a shift in the image that can be easily detected by a CCD array allowing for sub-wavelength accuracy of surface measurements. In our case, this method proved to be ineffective due to erroneous back reflections from other surfaces within the

prism. We determined the classic Hartmann test was the easiest and most effective way to measure the wavefront deviations introduced by an OST HMD as it could accurately measure both high and low sloped portions of the wavefront simultaneously with relatively basic optical components. Navarro and Moreno-Barriuso [16] were able to show how the Hartmann test accuracy can be greatly improved by increasing the distance between the Hartmann mask and the view screen distance. Liu and Huang et al. [17] were able to reduce the overall affects of noise in the measurement by increasing the sampling density of their Shack-Hartmann test with a scanning lenslet array approach to achieve measurements with 0.094 micron RMS error. We combine both of these methods to achieve similar results without the need of an expensive lenslet array.

3. Modeling Depth Distortion

3.1 Depth Distortion Background

The most obvious distortion in an optical system is the standard 2-D XY distortion that causes stretching or pinching of an image. However, even a perfectly flat or corrected optical element will inevitably introduce a 3-D depth distortion causing a perceived change in the viewing distance. Figure 5 below shows how a plane parallel plate introduces a depth shift causing the object to seem closer than it actually is. Light rays from a physical object point p (shown in RED) are refracted by a plane beamsplitter with a finite thickness before reaching they eye pupil. As a result, the refracted rays (shown in BLUE dashed lines) appear to intersect at point p' instead. This illustration is equivalent to the see-through path of a monocular OST-HMD, while the apparent

position of an object point to the eye is displaced to p’ due to the ray refraction through a plane parallel plate.

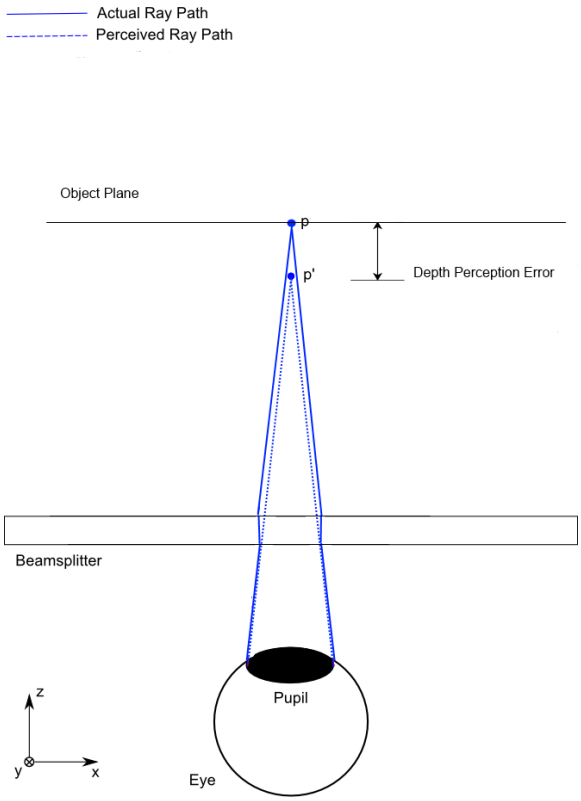

Figure 5. Accommodation shift introduced by a plane parallel plate when the object is viewed on-axis

In a binocular OST-HMD, two eyes typically view the object p through two separate beamsplitters which may be tilted relative to each other to keep the system symmetrical about the nose of the viewer. The convergence or the intersection of the perceived ray paths through the two beamsplitter plates for each eye provides the depth cue and creates the perceived position p’. Although the magnitude of the ray displacements by each beamsplitter is similar to that in a monocular case, the perceived depth error (p’-p) is usually more prominent than the monocular perception error due to

the typically different orientations of the beamsplitters and this is the dominant factor contributing to depth distortion caused by the beamsplitter. Figure 6 below shows an object being viewed by two beamsplitters tilted by equal but opposite angles. The perceived object point p' appears much farther than the actual object location p with a depth perception error of (p-p'). The magnitude and the direction of the error not only depend on the thickness of the beamsplitters, but also on the tilting angles and the tilting directions of the beamsplitters as well as the viewing direction of the object point with respect to the eye.

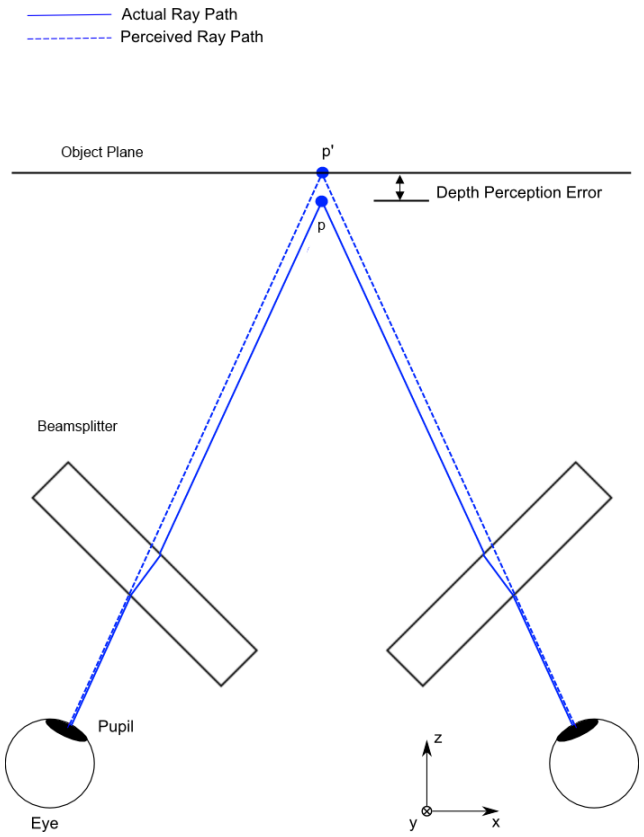

Figure 6. Shows how the ray paths in a stereo viewing system is affected by plane parallel plates.

For the rest of the chapter, a ray tracing method is described to determine the perceived distance error of an object in relation to the beamsplitter configurations. For both monocular and binocular configurations, we first examine the depth distortion caused by a plane parallel plate as a function of tilt, thickness, interpupillary distance (IPD), viewing angle, and object distance. We then proceed to investigate the depth distortion caused by combiners consisted of more complex surface shapes such as a freeform prism design shown in Figure 4.

3.2 Monocular Depth Distortion of a Plane Parallel Plate

Figure 7 shows an example of a ray trace through a 10mm PPP with a refraction index of 1.5 (surfaces shown in blue solid lines). The PPP is located at 25mm from the eye pupil, which corresponds to a typical eye relief in HMDs. The eye pupil is placed at the origin of the coordinate system OXYZ, the Z-axis is along the viewing direction, and the X-axis is parallel to the direction of interpupillary separation. The object plane is shown in green and is set at a given distance. For instance 50mm was arbitrarily chosen in this example to make the diagram easier to view. The object plane subtends an angular size of ±45° from the eye, which represents a typical range of see-through field of view (FOV).

A ray tracing program (e.g. Zemax, Code V, or MATLAB) was used to trace rays from the eye pupil of the observer through an optical element and into object space. To avoid tracing redundant rays from the object which may miss the eye pupil, rays were traced backward from the four edge points of eye pupil. Two of the edge points are in the YOZ plane which defines the marginal rays in the tangential plane, while the other two

edge points are in the XOZ plane defining the marginal rays in the sagittal plane. These marginal rays for different viewing angles are defined with uniform angular spacing when leaving the edge of the eye pupil. The ray tracing software traces a 10,000x10,000 grid of refracted rays into object space. The object plane is arbitrarily defined by a 21x21 grid of points (as seen in Figure 8) with uniform geometric spacing. Figure 7 only shows five object points in the X-direction to make the graphic easier to view. The location of each ray trace at the object plane is calculated and the ray most closely intersecting with each of the 21x21 object plane reference points is determined, these rays define our actual ray paths (shown in red in Figure 7). This ray tracing method allows us to determine the distortion map for a uniformly spaced object plane, which is more useful in real world application as your object plane is most typically a pixilated display. If you were to instead take a 21x21 array of rays with uniform angular spacing the result would be a distortion map for a distorted object plane.

The view angles of the actual ray paths between the origin and the first PPP surface are traced back into object space and shown below as dotted black lines. These rays are traced in 3D space. When the rays contain a Y-angular component, the two marginal rays will not perfectly intersect in the object space. When tracing the perceived ray paths back into object space we defined the minimum distance between two marginal rays as the best focus.

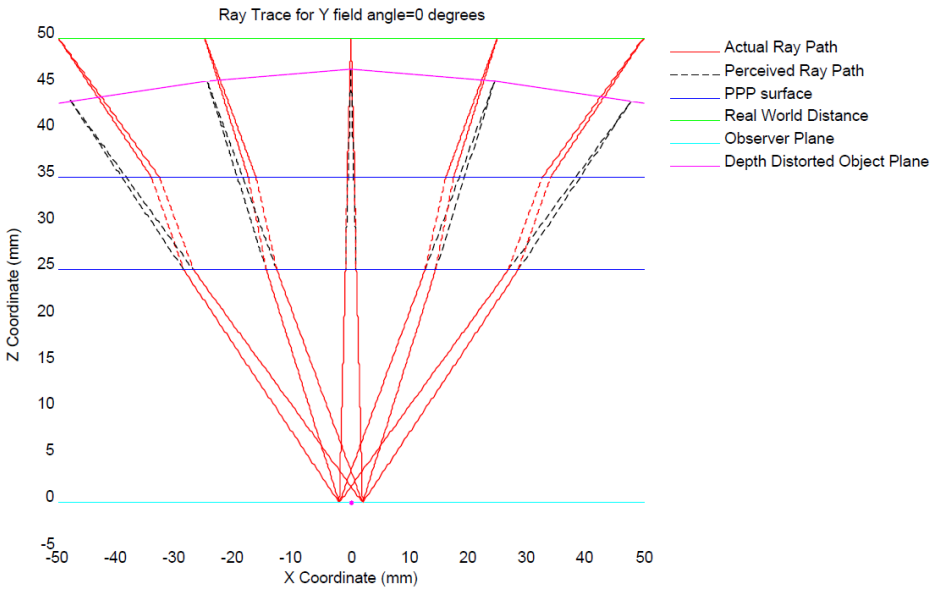

Figure 7. A single eye viewing an object at a distance of 50mm through a PPP of 10mm thickness

The best focus of these rays determines the perceived distorted object plane (magenta line) as a result of both XY and Z Distortion. The 10mm plate causes the observer to see the object 3.33mm closer on-axis in comparison to the actual object location. This is as expected as a PPP of index 1.5 will introduce an image shift of 1/3 the PPP thickness. The magnitude of the Z distortion increases as you go towards the edge of the field of view to a maximum value of 7.85mm as shown below in Figure 8. Figure 8 shows the 3D distortion for a 10mm PPP as both a function of the X and Y object position (21x21 object grid). There is no tilt to the PPP and the eye is centered within FOV so the distortion map is rotationally symmetric.

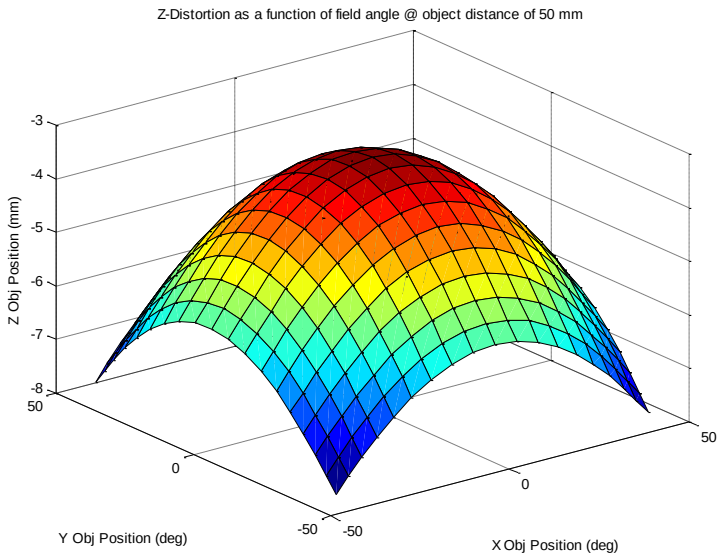

Figure 8. Z distortion as a function of field angle for a 45 degree HFOV

The depth distortion is proportional to the thickness of the PPP. A 20mm PPP exhibits exactly twice as much depth distortion as a 10mm across the entire FOV as seen below in Figure 9.

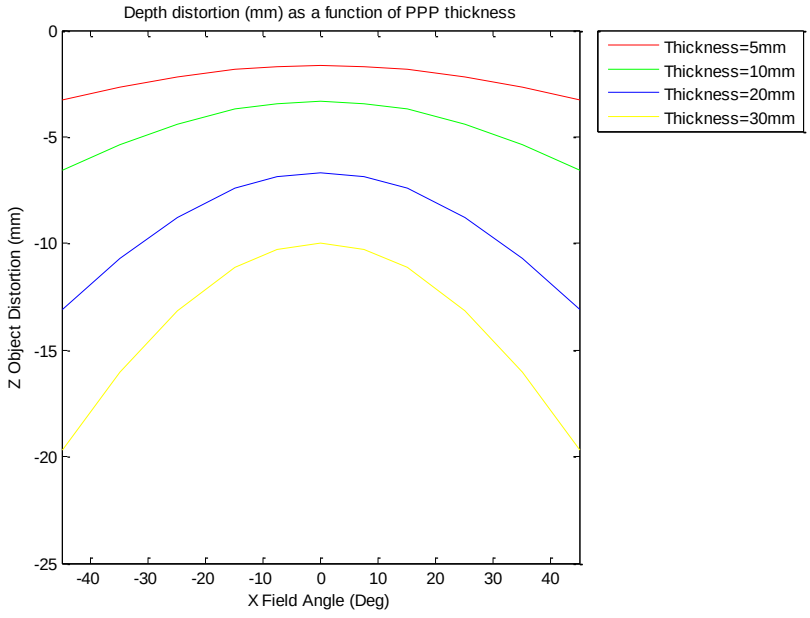

Figure 9. Depth distortion as a function of PPP thickness

It is worth noting that for a specific field of view the depth distortion is not affected by the pupil size, eye relief, or object distance, so at further object distances the Z distortion is less apparent and smaller in magnitude when measured in Diopters. This is shown below in Figure 10 (left) and Figure 10 (right). Both figures show the depth distortion as a function of field angle and object distance, but when the distortion is measured in millimeters (left) all 6 object distance curves overlap.

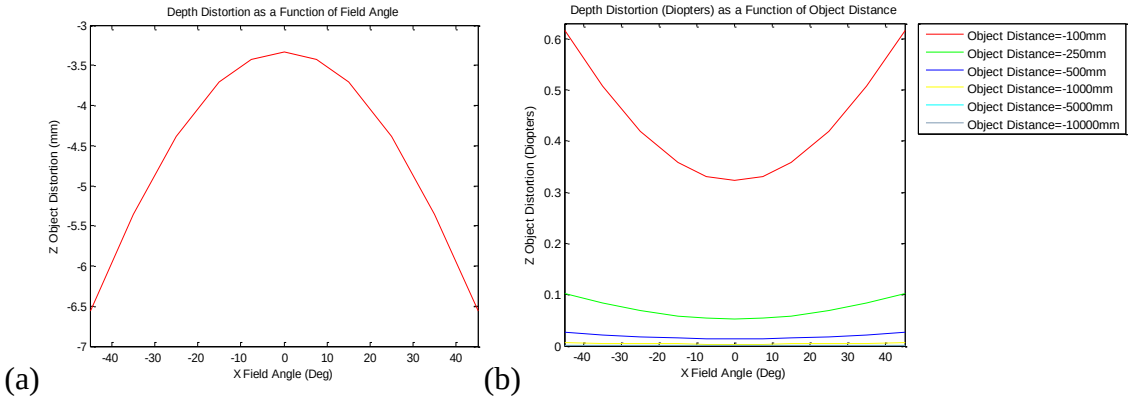

Figure 10. (a) Depth distortion measured in mm (b) depth distortion measured in Diopters

By examining the angles between the perceived object points and the actual object points we were able to define the 2D angular distortion of our object plane. This angular distortion map for this 10mm PPP and object distance of 200mm is shown below in Figure 11. The angular distortion of the object plane increases as you increase the field angle. The vector plot below shows the angular distortion is 0 at the center of the FOV and reaches a maximum value of 0.921 degrees at the corner. The 2D distortion is constant when measured in millimeters, so the angular distortion will scale inversely with the object distance.

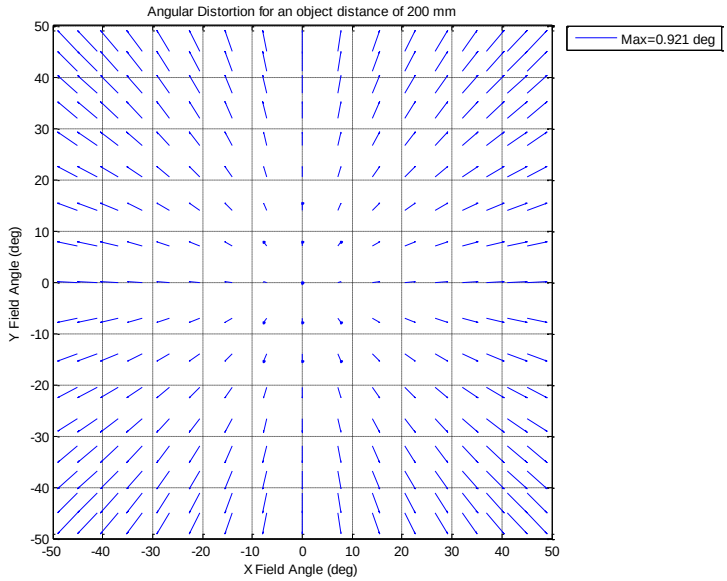

Figure 11. Vector plot showing the magnitude of the of the angular distortion across the field of view

Figure 12 shows the depth distortion as a function of FOV and tilt angle for a 10mm PPP and an object distance of 500mm. Tilting of the PPP causes a lateral shift in the depth distortion curve as seen below. Tilting the PPP by a specific angle will shift the curve along the x-axis by roughly the same angle. Tilt and viewing angle affect the depth distortion in the same way as they are purely a change in references. However the minimum Z Distortion decreases in magnitude as the tilt is increased because this distortion is measured as a projection along the Z-axis. The tilting of the PPP effectively makes the PPP thickness increase.

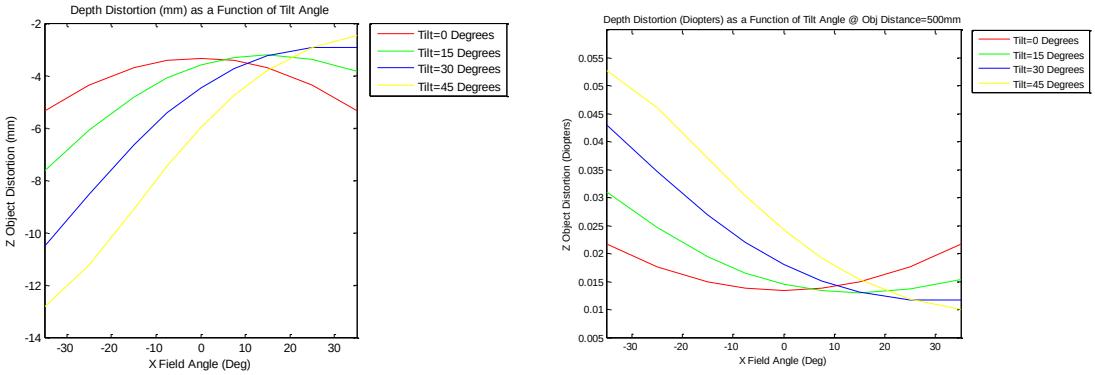

Figure 12. (left) Effects of PPP tilt on Z distortion (mm) for object distance of 500m (right) Z distortion measured in Diopters

3.3 Binocular Depth Distortion of a Plane Parallel Plate

The same ray trace method can be similarly used to look at the effects on binocular depth distortion. In the previous section we traced two marginal rays at the edge of a 3mm pupil. Now we are tracing two chief rays from two eyes separated by the interpupillary distance, which ranges from 54mm to 74mm for 95% of the population. Typically in a binocular AR display setup the system geometry is mirrored about the nose of the observer as shown below in Figure 13. As a simple example, Figure 13 shows two eyes with a 64mm IPD viewing an object plane at a distance of 100mm. The eye clearance measured at the center point between the eyes is 25mm. Each 10mm PPP beamsplitter is tilted at ±7 degrees. The object plane located at a distance of 100mm appears 2.5-4mm closer to observer when viewed through this geometry.

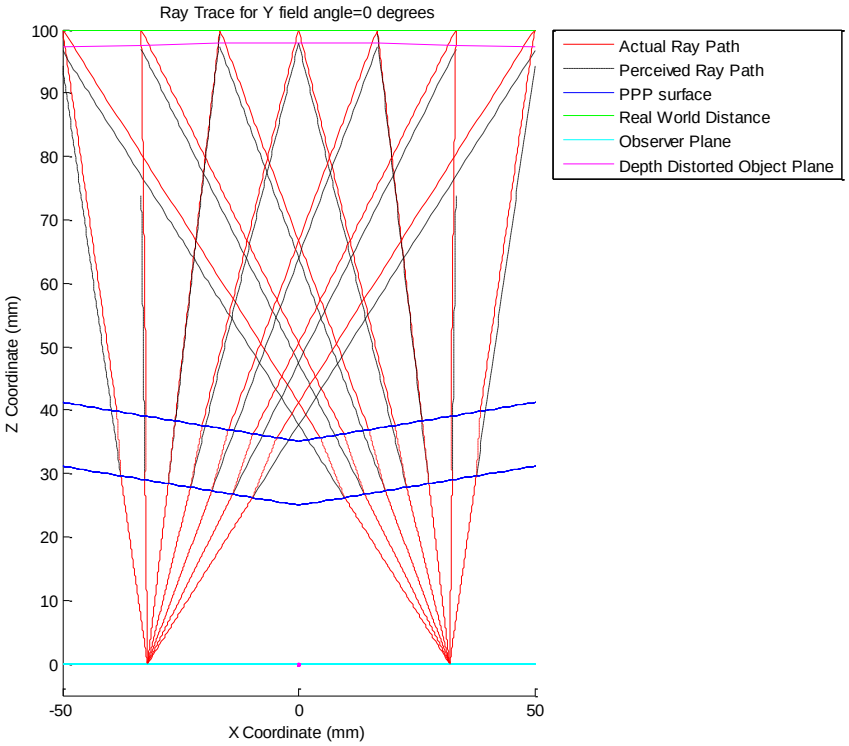

Figure 13. Binocular setup examining effects on convergence, 7 degree tilt, 64mm IPD

Figure 14 shows the Z distortion as a function of PPP tilt angle in a binocular setup. For an object distance of 500mm and a PPP thickness of 5mm, the on-axis distortion is as high as 22mm at a tilt angle of 45°, which is much larger than the magnitude of errors for non-tilted PPP in binocular configurations or for tilted PPP in a monocular configuration. When the prisms are tilted at 3.66 degrees they are perpendicular to the viewing axes as defined by the IPD and the actual object location and we observe zero depth distortion. This is to be expected as there is no ray deviations introduced at normal incident angels. Note that while there is no binocular depth distortion in this specific instance, each individual eye will still experience a monocular shift of 1.66mm as described in the previous section. The teal curve showing the results

for a tilt angle of 0° is identical to the monocular results for a non-tilted PPP, as the 64mm IPD behaves as a single pupil with a 64mm pupil. The magnitude of the depth distortion scales with the prism thickness.

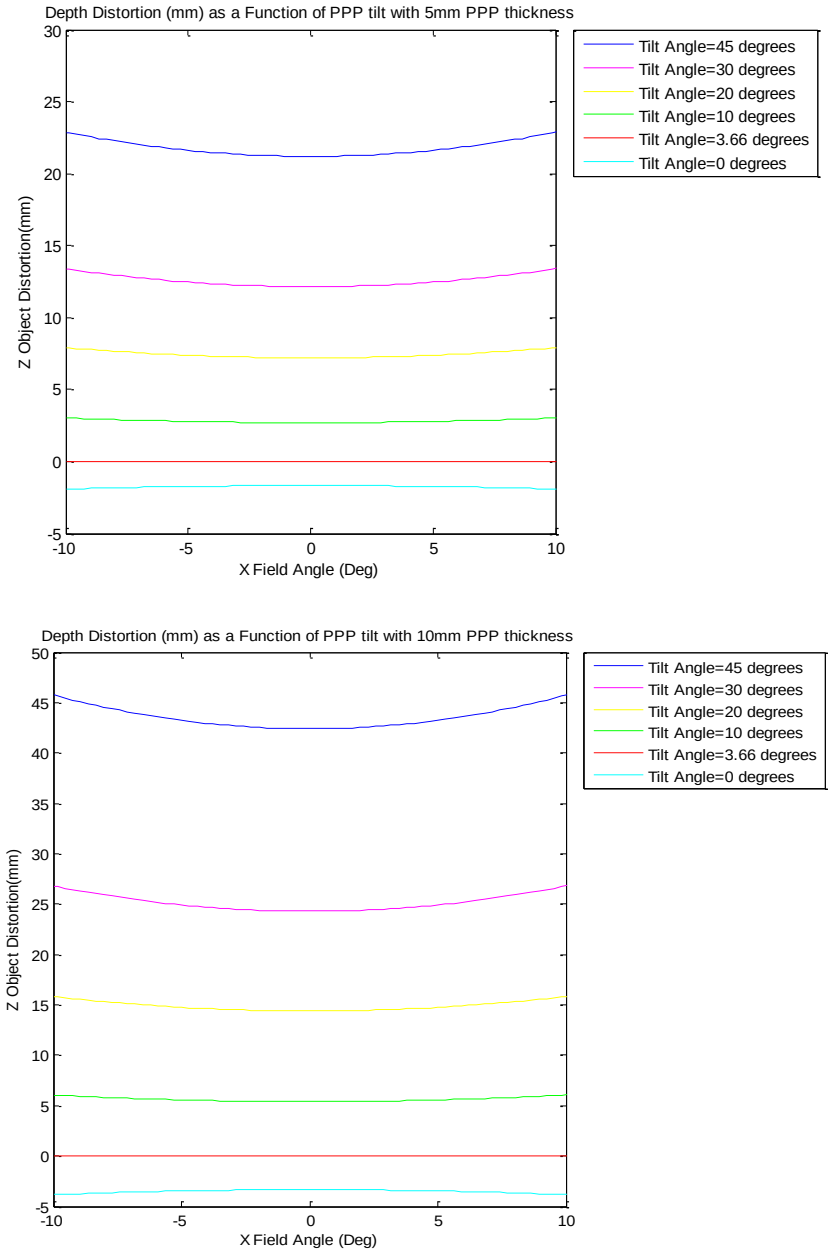

Figure 14. (top) Z distortion as a function of PPP tilt with PPP thickness of 5mm and (bottom) Z distortion as a function of PPP tilt with PPP thickness of 10mm

Figure 15 shows the effect of IPD on the on-axis Z distortion. The smaller IPD increases the magnitude of the binocular depth distortion due to the viewing angle being further from perpendicular. Wong et al 2002 [21] found the average human stereoacuity to be about 40 arcseconds, which equates to depth distortion of 1.5mm for an IPD of 64mm and and object distance of 500mm. This means a PPP tilt greater than 10 degrees will cause a noticeable focal shift for the viewer.

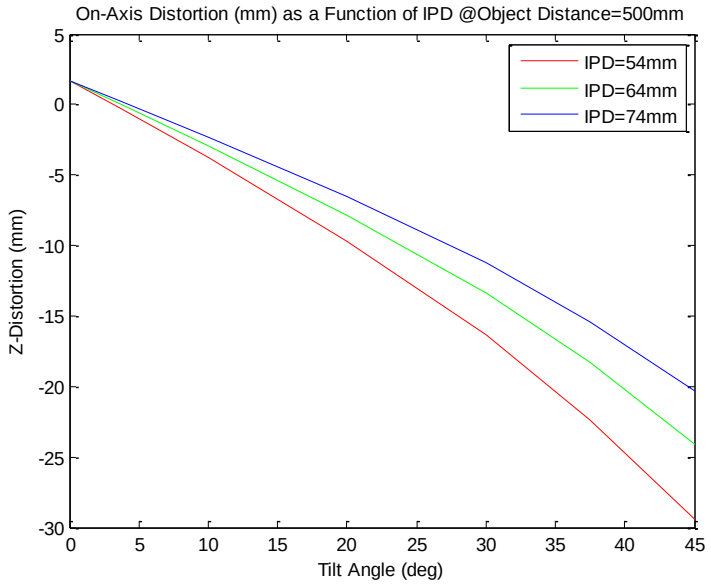

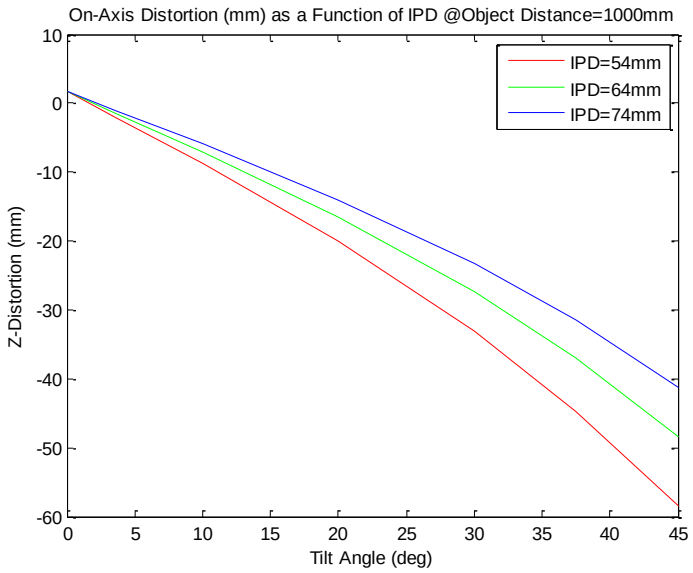

Figure 15. (top) Z distortion (mm) as a function of IPD with 5mm PPP thickness at object distance of 500mm (bottom) Z distortion (mm) as a function of IPD with 5mm PPP thickness at object distance of 1000mm

The two graphs in Figure 15 demonstrate how the depth distortion scales linearly with the object distance. In Figure 16 we have the same two graphs but the depth distortion is measured in Diopters. At further object distances the perceived distance change is a smaller change in power.

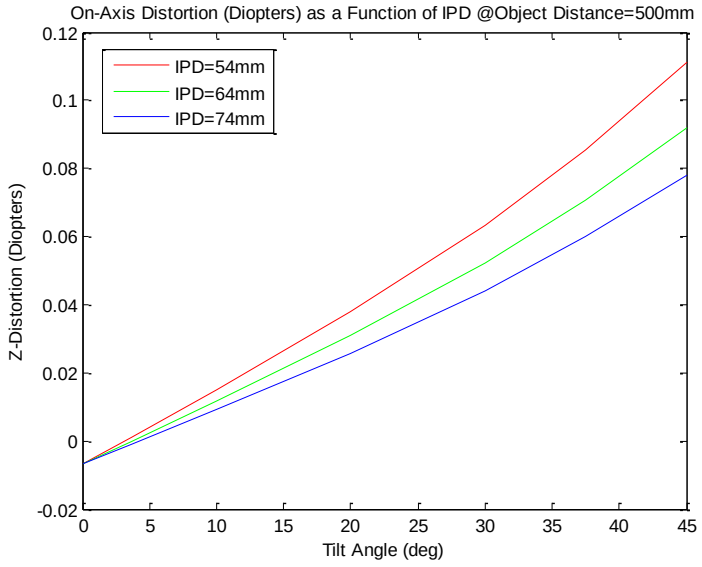

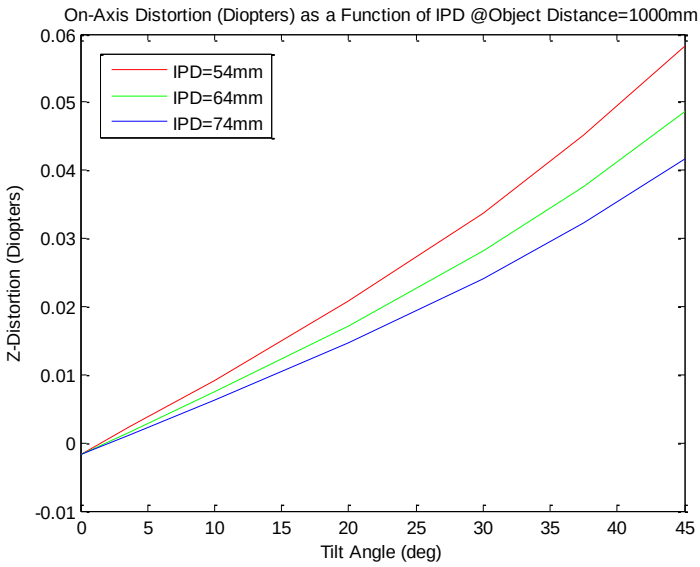

Figure 16. (top) Z distortion (Diopters) as a function of IPD with 5mm PPP thickness at object distance of 500mm (bottom) Z distortion (Diopters) as a function of IPD with 5mm PPP thickness at object distance of 1000mm

3.4 Depth Distortion in a freeform OST HMD Prism

Recent advances in the manufacturing processes of precision plastics have made it easier for optical system designers to take advantage of freeform (non-rotationally symmetric) surfaces. Diamond turning, high precision molding, and 3D printing allow freeform surfaces to be manufactured more cheaply and easily than ever before.

Our ray trace method can similarly be used to predict the depth distortion introduced by more complicated geometries as seen in a freeform OST HMD prism. Here we examined the effects on depth distortion of a freeform eyepiece prism with a structure similar to the one shown in Figure 4. It is a custom-designed freeform prism designed for an eyetracked head-mounted display system, the details of which can be found in Hua et al [20]. The freeform prism with the compensator lens has a total

thickness of 18.25mm, made from plastic with an index of 1.52. A PPP of this thickness would produce an on-axis depth distortion of -6.25mm. Figure 17 below shows the depth distortion as a function of the X field angle at distances of 1000 and 2000mm, respectively for a 12mm pupil, . The simulation examines the eyepiece at the designed eye relief of 21mm and a 30degree horizontal FOV. The 12mm pupil results in Figure 17 show at an object distance of 1000mm the on-axis depth distortion is approximately 232mm for the meridional focus and 636mm for the sagittal focus. This corresponds to a residual negative power with a magnitude of about 0.2-0.4 Diopters. This residual power contributes to a larger amount of depth distortion at farther object distances. At an object distance of 2000mm, the eye would be viewing the object with 0.5 Diopters. The -0.4 Diopters of power in the sagittal direction almost completely cancels the eye accommodation and pushes the focus out to 9300mm corresponding to 7300mm of depth distortion. The meridional focus is shifted by about 1250mm.

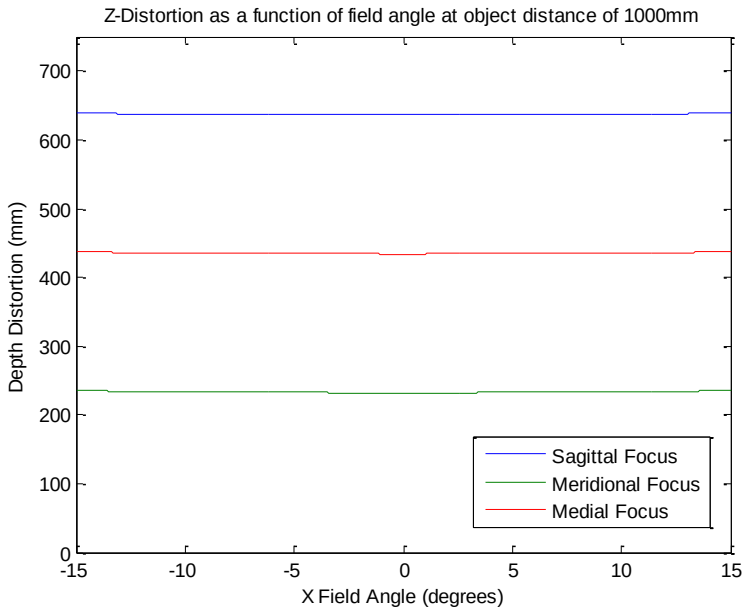

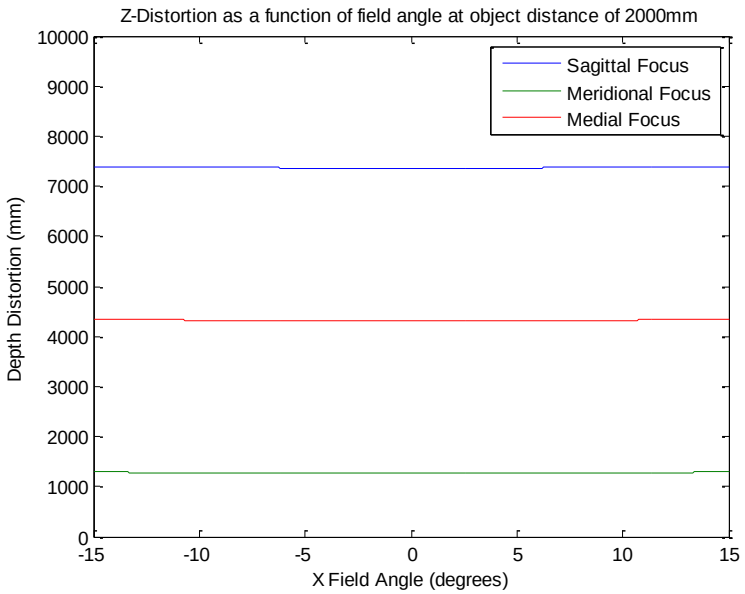

Figure 17. (top) Z distortion plot for freeform prism with a 12mm pupil as a function of X field angle for an object distance of 1000mm and (bottom) Z distortion plot for freeform prism for an object distance of 2000mm

Figure 18 shows the same Z-Distortion plots as Figure 17 but with a 3mm pupil. The eyepiece demonstrates some spherical aberration, with there being about half as much power across a 3mm diameter pupil, roughly -0.1 to -0.2 Diopters.

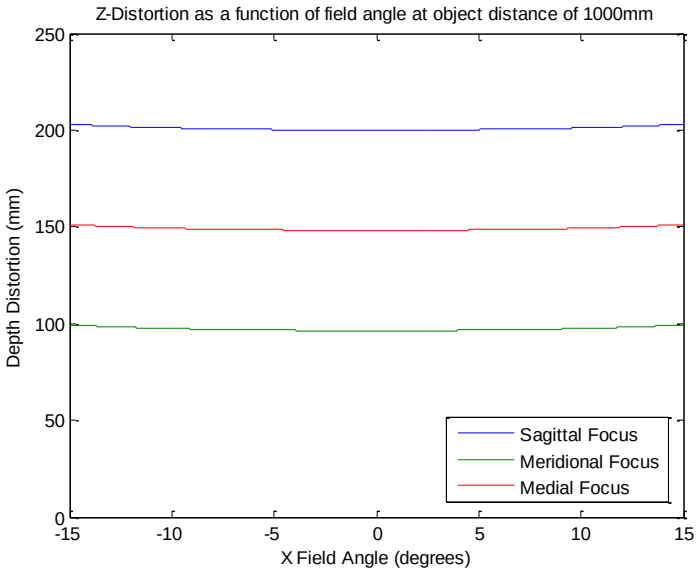

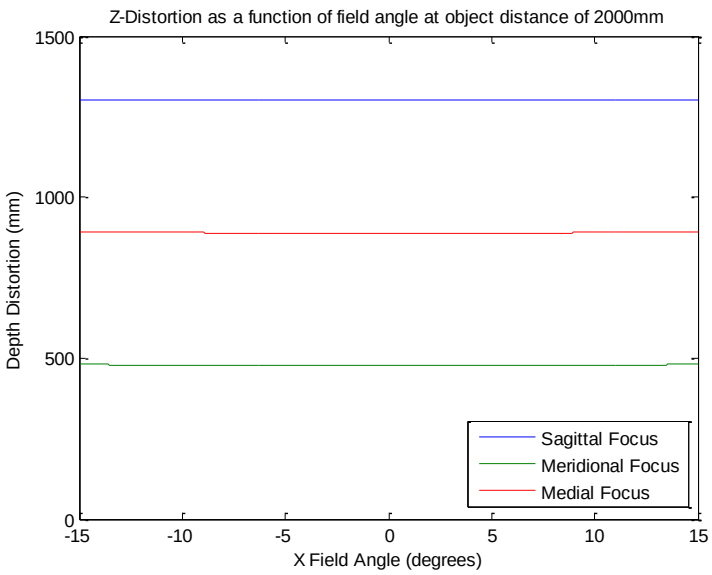

Figure 18 (top) Z distortion plot for freeform prism with a 3mm pupil as a function of X field angle for an object distance of 1000mm and (bottom) Z distortion plot for freeform prism for an object distance of 2000mm

4: Hartmann Wavefront Testing

4.1 Hartmann Testing Background

The Hartmann test consists of an array of apertures to sample the wavefront and examine the wavefront slope at fixed points at the Hartmann mask location [5]. Traditionally this method uses an opaque mask with a pattern of holes, each of which allows a thin pencil of rays to pass through and project a spot on a viewing screen or CCD array. Two images are captured, a calibration image to determine the projected spot pattern from collimated light and then a test image with the test piece in place produced new spot locations. The spot shifts introduced by the test piece determine the wavefront slope at each hole location. The wavefront shape is then determined through

numerical integration of the measured wavefront slope. This method is versatile in that you can customize your hole spacing and view screen distance to effectively measure either high or low powered wavefronts. Low powered wavefronts need highly sampled measurements with long viewing distance to accurately measure the small wavefront deviations while high powered wavefronts need less sample points to eliminate any overlap amongst the projected spots.

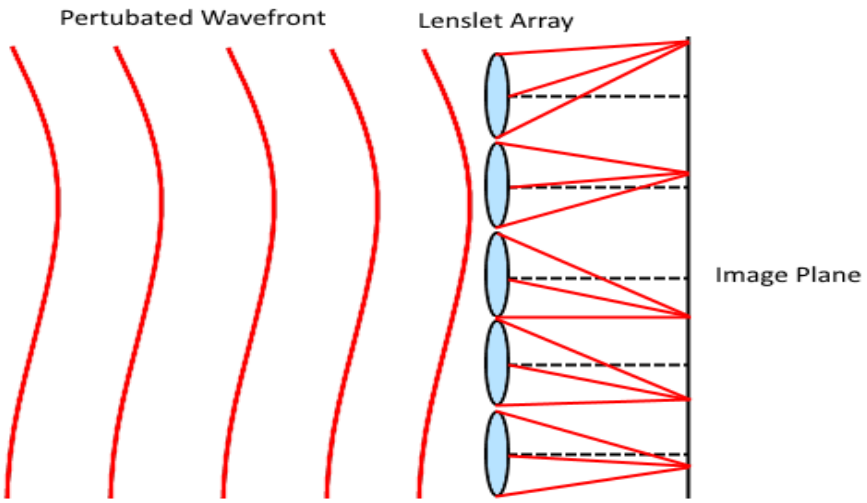

Figure 19. A Shack-Hartmann test showing how the focal points of each lenslet shift with relation to the local wavefront slope

With advances in manufacturing of precision plastic optical elements, the Hartmann mask has been commonly replaced with custom made lenslet arrays that focus each spot onto the viewing screen or CCD array (Figure 19). This modification to Hartmann test is commonly referred to as the Shack-Hartmann wavefront test [5].

Minimizing the spot size typically reduces the centroiding errors which is usually the largest source of error.

In this paper, we developed a Hartmann wavefront testing setup to test the wavefront error produced by a see-through freeform eyepiece with compensator using a low-cost opaque mask and a CCD sensor. We achieve similar levels of accuracy with cheaper and easier to manufacture opaque masks by increasing the view screen distance to longer distances [6]. At these larger viewing distances the minimum diffracted spot size is comparable to the hole size of the mask and a focusing lenslet array no longer provides any advantage. We further increase the accuracy by scanning the Hartmann mask across the aperture at fine steps, which effectively increases the sampling density of the wavefront without reducing the size and brightness of each spot [7]. By combining both the scanning mask and the longer view screen distances we are able to characterize wavefronts with high levels of accuracy. The testing accuracy is verified using both high power and low power lenses. The error of these measurements is shown to be less than 0.2microns Peak-Valley. We then measured the more complex wavefront of a freeform optical-see-through prism. The results are compared to the theoretical wavefront as simulated by ray tracing software, and the difference between the two reveals the wavefront deviation introduced by manufacturing errors in the prism. We replicated this wavefront deviation in our ray tracing software to estimate the amount of decenter and tilt present in our system. We also use our testing setup to test the OST prism at obscure viewing angles to fully characterize the wavefront distortion as seen in real world use.

4.2 Eyetracking Freeform OST HMD prism

The OST HMD design discussed and tested throughout this paper is the same freeform eyepiece analyzed in Section 3.3 and designed by Hong Hua et al [8]. The imaging principles of the OST HMD prism were described earlier in Figure 4 but with an added eye-tracking camera sharing the virtual display path that isn't relevant to this paper. Figure 20(left) shows the optical design layout of the prism design for both the virtual display and the see-through path through a freeform corrector lens. The main focus of this study is to evaluate the wavefront distortion induced by the cemented prism and corrector to the direct see-through view of a real-world scene, which is closely related to the resulting depth perception error discussed in Section 3.3. The MTF field plot for the see-through path of this design is shown below in Figure 20 (right). The green circles show an average contrast of 0.17 across the 40ºx30º FOV at 1arcmin resolution, which is the often quoted angular resolution limit of the human eye, demonstrating that the system is well corrected and introduces minimal blur to the real world view. However, the system thickness is roughly 18.25mm and this inevitably causes significant amounts of wavefront distortion to rays passing through the system.

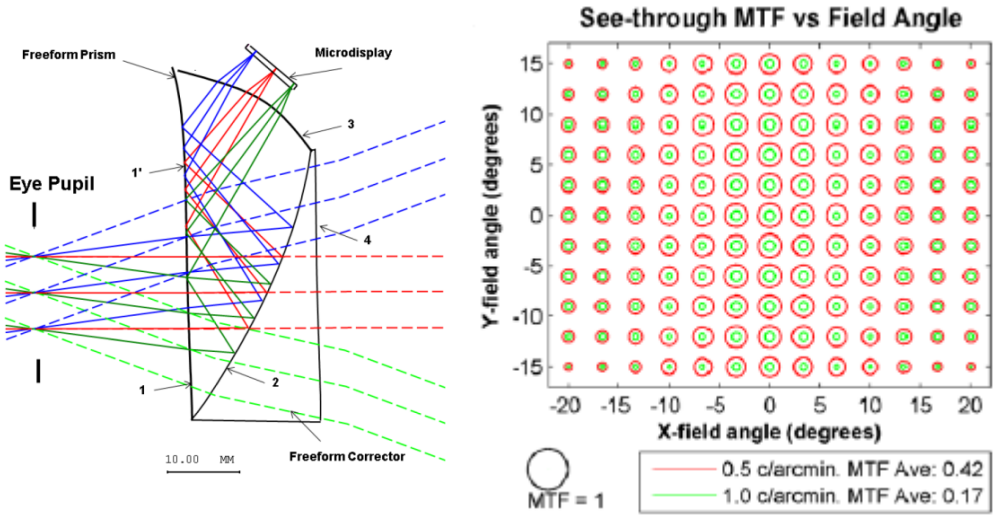

Figure 20. Eye-tracking OST HMD with its corresponding MTF field plot [20]

As with any optical element with high tolerance surface parameters, small manufacturing errors can cause significant changes to the optical performance of a system. In order to best calibrate for the 3D distortion induced by a freeform OST-HMD we need to quantify post-production manufacturing errors. The highly sloped freeform surfaces commonly used in OST-HMD designs typically present a challenge for most surface testing techniques. Our objective is to apply a classic Hartmann test to test these wavefront errors easily and accurately.

4.3 Testing Setup

The Hartmann test setup consists of a collimated source being expanded through a test piece and Hartmann mask, projecting an image on to the viewing screen. We chose a 650 nm laser diode as our testing source. A 40x microscope objective combined with a 300mm collimating lens allowed us to overfill the 12mm pupil with uniform illumination. The beam collimation is confirmed using a 2" wedge shear plate

interferometer (Melles Griot, Part Number 09 SPM 003). The residual beam divergence was measured to be larger than 5.6km, which corresponds to a residual optical power of 0.000179 D. To simulate the actual use of the eyepiece, a pupil was placed at the prism's designed eye relief of 21mm from the front surface and centered about the rotation axis of a rotation stage as shown in Figure 21(b). This gave us the ability to test off-axis viewing angles for a fixed pupil position. This paper will show the results of 5 different viewing angles; (0˚,0˚), (12.5˚,0˚), (-12.5˚,0˚), (0˚,11˚), and (0˚,-11˚).

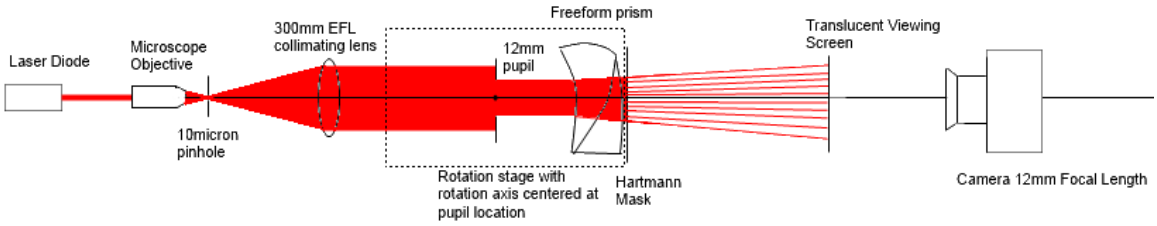

(a)

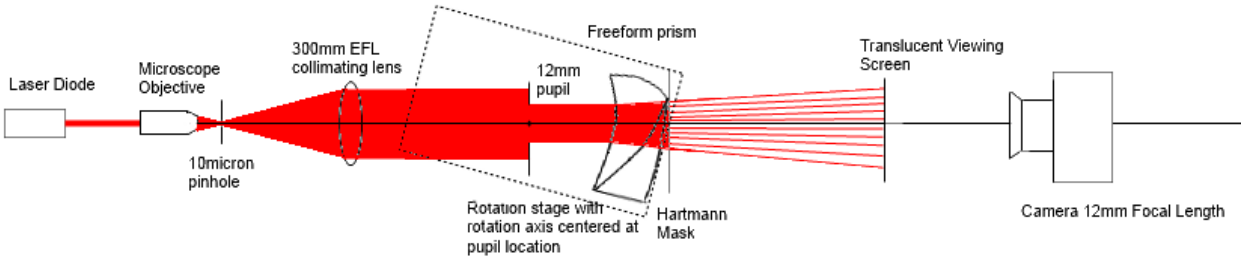

(b)

Figure 21. (a) Testing layout with on-axis viewing angle (b) Testing layout with tilted viewing angle

The viewing screen was a piece of ground glass allowing the projected spot pattern to be viewed by a camera from behind the viewing screen. Trying to view the screen from the front required off-axis viewing which would introduce keystone distortion to the

pattern or the use of a beamsplitter which would need to be carefully aligned and reduces the spot brightness.

The Hartmann mask shown in Figure 22 has 1mm holes with 1.5mm spacing. This combination was chosen to maximize the amount of sample points within the 12mm pupil while minimizing the effects of diffraction and cross-talk between adjacent holes. Placing the viewing screen 600mm from the mask, the diffraction limited spot size of lenlet array was estimated to be 0.95mm, approximately equal to the hole size. Minimizing the spot size can help to increase the accuracy of the spot centroiding.

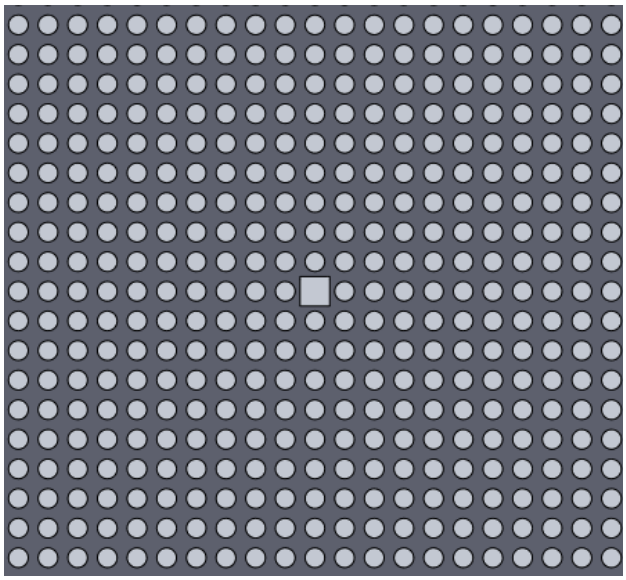

Figure 22. Hartmann mask with 1.5mm hole spacing

The maximum measureable slope is limited when two spots overlap at the viewing screen. 1.5mm spacing allows for a maximum wavefront slope change of 1.5mm/600mm=0.0025 for each hole spacing of 1.5mm, which equals to 0.143 degrees

of surface normal deviation. This equates to 0.00167/mm which is greater than the maximum slope change induced by our prism under test. The square hole in the center of the mask is used as a reference point to help match the corresponding spots in each image during the image processing.

We placed the Hartmann mask on an X-Y micrometer translation stage allowing us to shift the Hartmann mask and sub-sample our aperture with 5micron repeatability. The precision of the translation gave us more sample points allowing higher accuracy when determining the wavefront shape without limiting our maximum measureable slope.

4.4 Sources of Measurement Error

Eq (1) below shows how the wavefront slope *W'* is related to the spot location in the image *u(p)*, the system magnification *S*, the normalized pupil coordinate ρ, the mask radius r_{max}, and the viewing screen distance *D*.

$$W' = \frac{u(\rho) \cdot S - \rho \cdot r_{max}}{D} \quad (1)$$

Eq (2) is the partial derivative of the wavefront slope with respect to the system magnification.

$$\frac{dW'}{dS} = \frac{u(\rho)}{D} \quad (2)$$

Eq (3) is the partial derivative of the wavefront slope with respect to the pupil location.

$$\frac{dW'}{du(\rho)} = \frac{S}{D} \quad (3)$$

Eq (4) is the partial derivative of the wavefront slope with respect to the mask radius.

$$\frac{dW'}{dr_{\max}} = \frac{-\rho}{D} \qquad (4)$$

Eq (5) is the partial derivative of the wavefront slope with respect to the view screen distance.

$$\frac{dW'}{dD} = \frac{-u(\rho)\cdot S + \rho \cdot r_{\max}}{D^2} \qquad (5)$$

Looking at the partial derivative shown by Eq's (2)-(5) we can see that increasing the view screen will reduce all of the sources of error in this measurement.

The 12.08mm aperture had a measurement accuracy of ±0.01mm when measured with a micrometer. At the view screen distance of 600mm, this introduces a slope error of 1.667×10^{-5}. This aperture was used as a reference to determine our system magnification. The system magnification of our setup is 0.0241 mm/pixel and our camera has a pixel size of 3.75microns. Imaging the aperture and counting the pixels with image processing software was the easiest way to determine the magnification. The 10 micron uncertainty in the aperture size combined with 3-4 pixels of uncertainty in determining the aperture edge led to a 0.2% uncertainty in the magnification, which contributes a slope error of 8.0372×10^{-8}. The view screen was placed on an optical rail; the view screen distance of 600mm was measured with an accuracy of ±1mm. This affects any wavefront slope measurement by a factor of 1/600 or 0.167%.

We examined a calibration image and the repeatability of our centroiding. The results from 2800 sample points are shown below in Figure 23. The standard deviation is 3.5 pixels or 13.125 microns of centroid error when measured at the camera CCD.

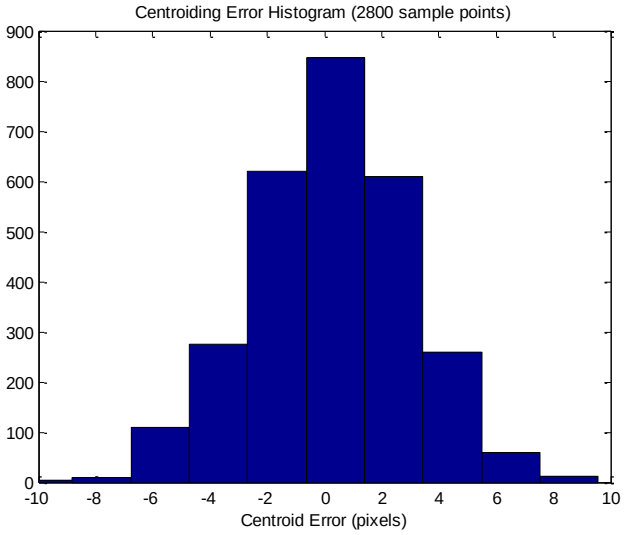

Figure 23. Histogram showing the distribution of centroid errors for 2800 sample points

At a view screen distance of 600mm, this centroid error corresponds to a slope error of 1.406×10^{-4}, which is the dominant source of error in our test. Because it is a random noise error its effect can be minimized by increasing the amount of sample points across the pupil. Our 12mm mask only has 81 holes, so we scanned our mask with a micrometer translation stage to subsample the aperture for 2800 unique sample points. We determined the relationship between the wavefront error and the number of sample points by testing a collimated wavefront against itself as a reference image, thus eliminating all sources of error except for the centroiding errors. This relationship is

shown below in Figure 24. Integrating the slope error produced a wavefront with a magnitude less than 1micron. This test was done with a view screen distance of 600mm.

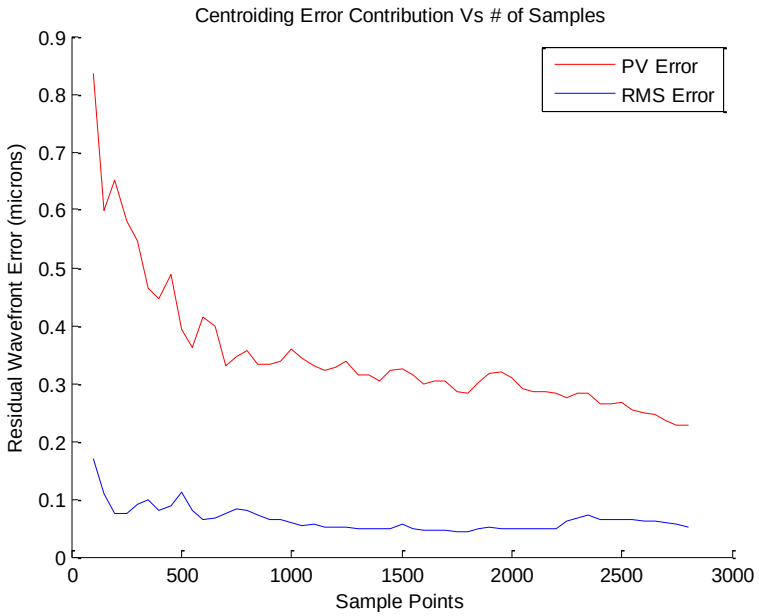

Figure 24. Graph showing the relationship between the centroiding error contribution and the number of sample points across a 12mm pupil at a 0.6m viewing distance

Sampling a 12mm diameter pupil 100 times resulted in a Peak-Valley error of 0.84microns. Increasing the number of sample points to 2800 reduced the Peak-Valley error to approximately 0.28microns. The point of diminishing returns occurs around 900-1000 sample points with a PV error contribution of approximately 0.33microns. Previous studies done by R. Navarro *et al* have shown comparable results using a Shack-Hartmann test with an RMS error of 0.094microns [16]. Figure 24 can provide insight when deciding how many sample points are needed. The centroid error provides a constant slope error, so a high powered wavefront with 1mm of sag will hardly be

affected by this noise and 100 sample points will be sufficient. While a relatively flat wavefront that needs better than 0.1micron accuracy and 2800 sample points with an increased viewing distance of 1.8m will be needed.

The collimation of the source was done with a 2" wedged shear-plate interferometer. The residual wavefront error of the collimation had a radius of 5.9km, which is much less power than any our measurements. The camera distortion was calibrated using the Cal Tech Calib Toolbox algorithm [19]. The algorithm finds the corners of an image containing a uniform grid and corrects for any observed camera distortion. The average residual pixel distortion error after correction was 0.33 and 0.27 pixels in the X-Y directions as shown below in Figure 25.

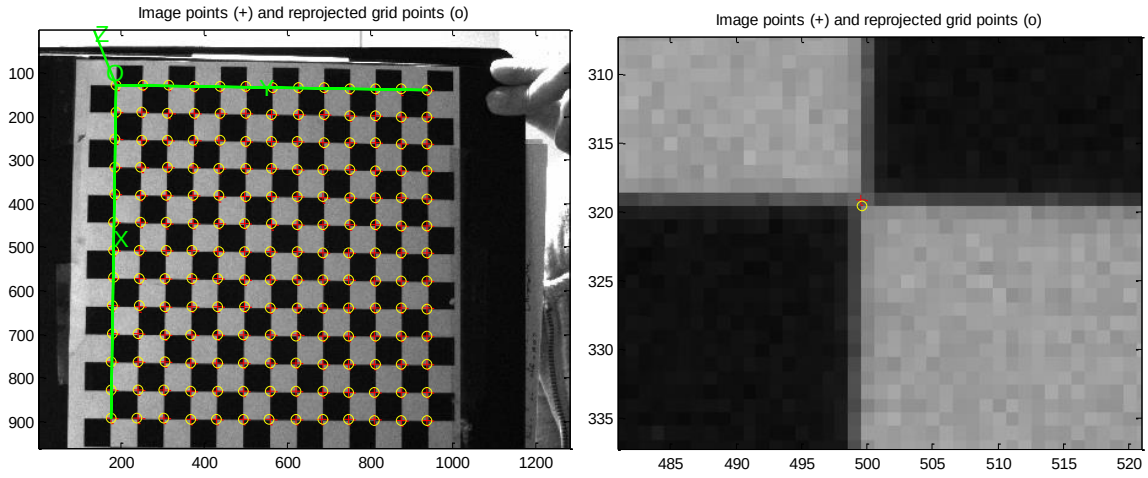

Figure 25. Shows the distortion software and residual distortion errors

The residual distortion is very small compared to our centroiding errors and because it affects both the calibration and test images it has almost no effect on the wavefront measurement.

4.5 Spherical Lens Tests

The testing setup as shown in Figure 21 was used to test a relatively high powered 800mm lens. Due to the fact that we were testing a converging wavefront, we had to reduce the view screen distance to 200mm to prevent spot overlap. This tripled our expected centroid error contribution. With 1000 sample points across a 13mm aperture we expected the centroiding error to contribute approximately 1micron of noise PV.

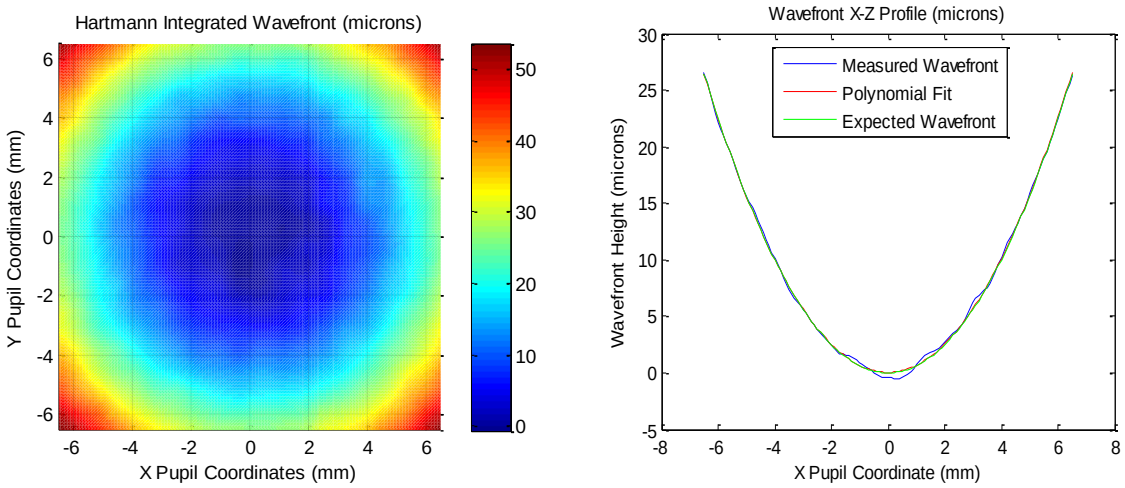

Figure 26. Wavefront measurement of an 800mm focal length lens (left) with the X-Z profile shown (right)

Figure 26 (left) shows the wavefront measurement of this lens with the X-Z wavefront profile being shown in Figure 26(right). The expected wavefront sag for an 800mm focal length lens was 26.41microns while the measured sag was 26.49 microns after applying a polynomial fit. Figure 27 below shows the difference between the expected shape and the measured wavefront shape. The error looks to be a random noise error resulting primarily from the centroid errors with a P-V magnitude of about 1.15microns, closely matching the noise as predicted in Figure 24.

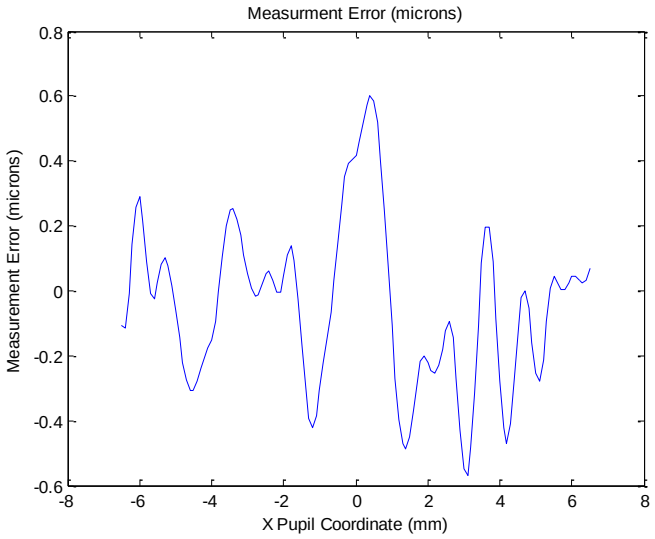

Figure 27. Wavefront measurement errors for an 800mm focal length lens

A 60m focal length lens was then measured to look at the accuracy when measuring a much flatter wavefront. The view screen distance was increased back to 600mm and we continued to use 1000 sample points. Figure 28 below shows how much more of an effect the centroid error has on a much flatter wavefront even with the longer view distance.

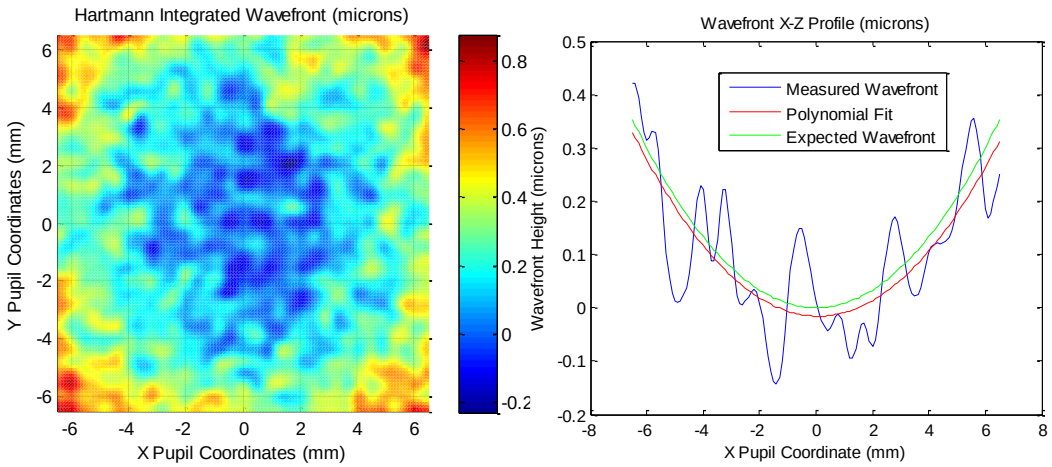

Figure 28. Wavefront measurement of a 60m lens at a view screen distance of 600mm (left) with the X-Z profile show (right)

The expected wavefront sag was 352.1nm while the measured sag after applying a polynomial fit was 382.2nm, an 8.544% error. The random noise introduced into our measurement is very significant as shown in Figure 28 and Figure 29.

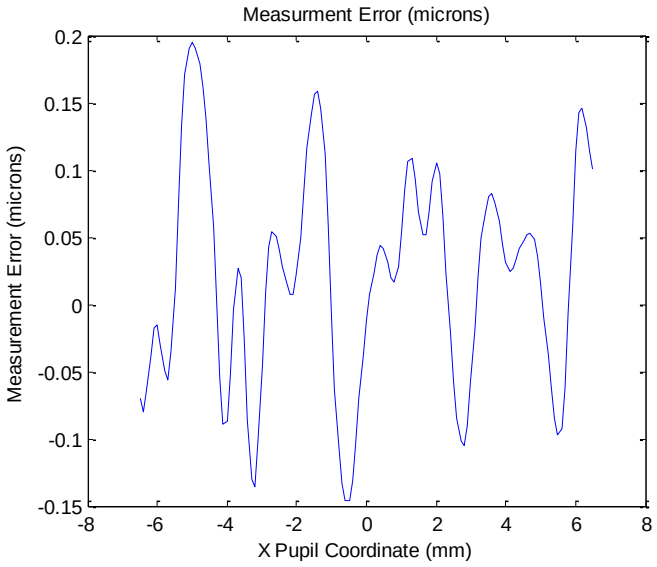

Figure 29. Wavefront measurement errors for a 60m focal length lens at a view screen distance of 600mm

We then repeated the same test with the viewing screen distance doubled to 1.2m attempting to halve the effects of the centroid errors. The results are shown below in Figure 30.

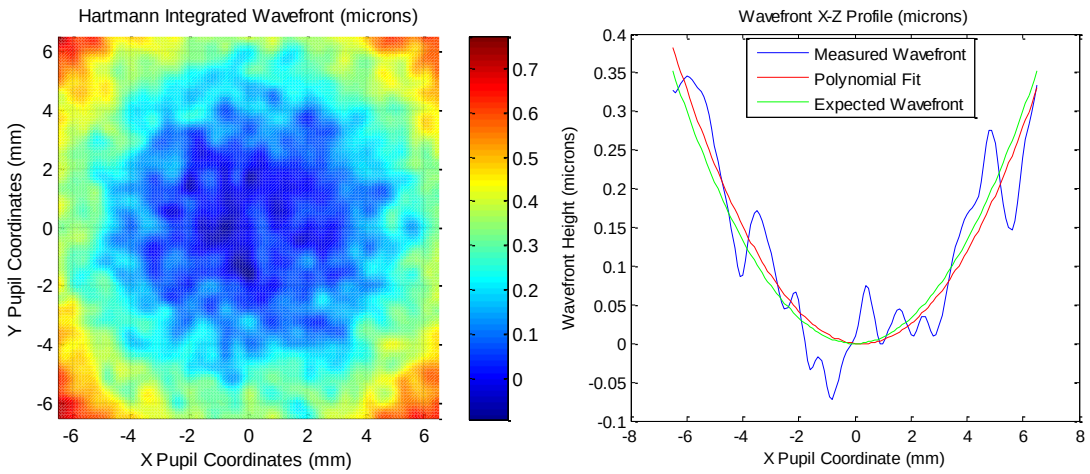

Figure 30. Wavefront measurement of a 60m lens at a view screen distance of 1200mm (left) with the X-Z profile shown (right)

The measured wavefront is much smoother. The polynomial fit still differs from the expected sag by about 8.5% but the SNR is much improved. Figure 31 below shows that increasing the view screen distance by a factor did roughly reduce the noise by a factor of 2 as predicted, resulting in a P-V noise of about 0.20 microns.

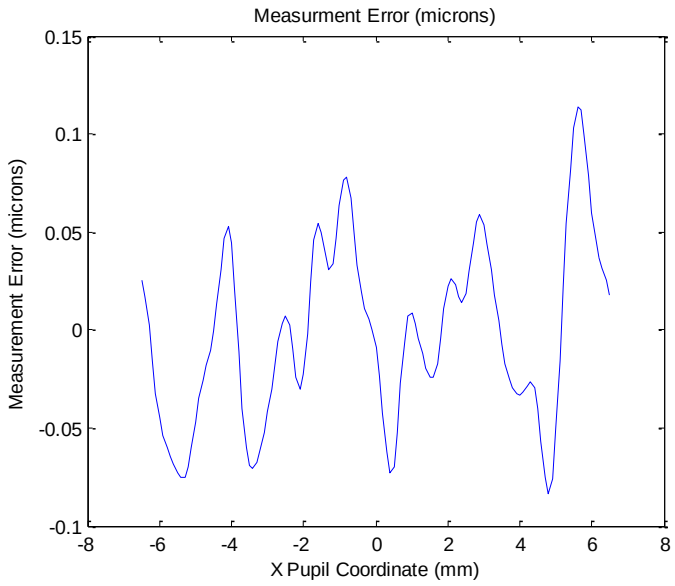

Figure 31. Wavefront measurement errors for a 60m focal length lens at a view screen distance of 1200m

4.6 Testing of a freeform prism

Using the same setup as shown in Figure 21, we tested the eye-tracking freeform OST HMD prism. The side profile of this prism with only the OST optical path is shown below in Figure 32.

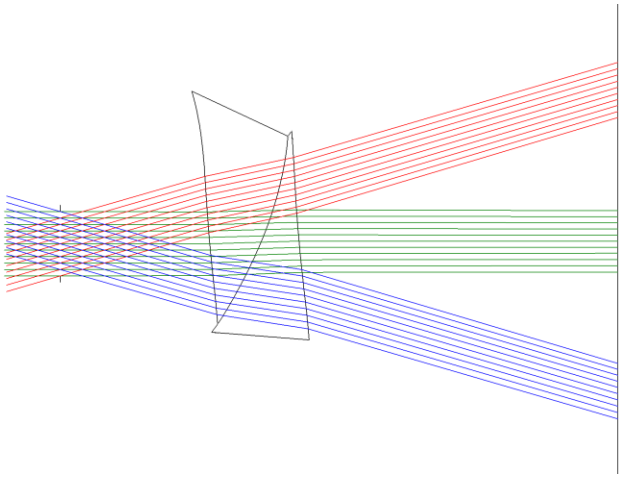

Figure 32. Optical layout for the freeform OST HMD prism used in our tests

The expected wavefront had a maximum sag of approximately 21 microns so we determined a view screen distance of 600mm and approximately 1000 sample points across a 12mm pupil would provide more than sufficient accuracy. The freeform prism was designed using the ray tracing program CodeV and the theoretical wavefront was calculated and used for comparison. The results of our test and the CodeV Theoretical Wavefront are shown side by side below in Figure 33. The sagittal and tangential best fit spheres for our measured wavefront have radii of 2.45m and 5.1m, respectively. This matches the expected power determined in our ray tracing simulation in Section 3.3 for a 12mm pupil. For a 3mm pupil the best fit spheres have radii of 5.2m and 9.8m in the sagittal and tangential directions, respectively.

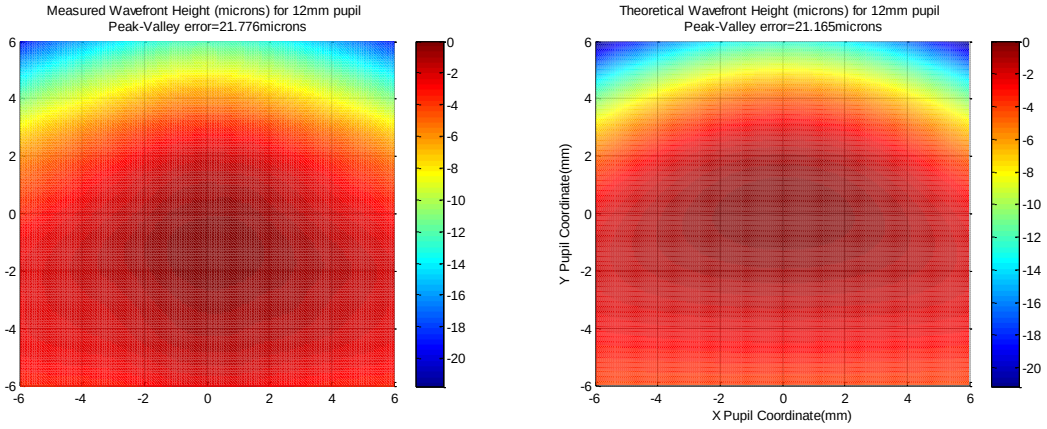

Figure 33. The measured wavefront of a freeform prism (left) compared to the theoretical wavefront (right)

The residual difference between measured and theoretical wavefronts is shown below in Figure 34. The residual PV difference is about 3microns, which is about 15% of the total wavefront deviation, significantly greater than our typical measurement error

caused by centroiding. The residual wavefront difference shows us the magnitude of the wavefront deviations caused by surface shape and decenters introduced by the manufacturing process.

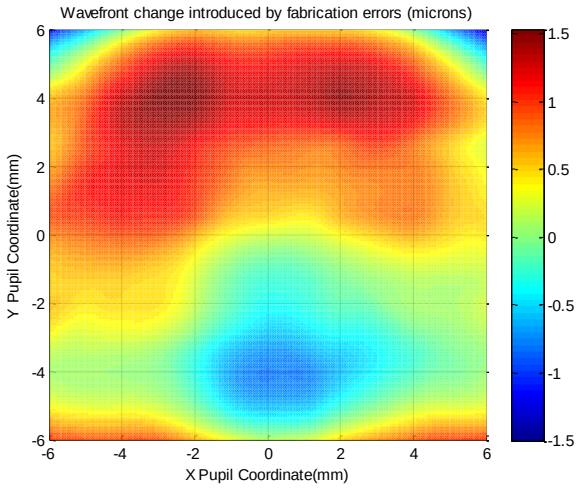

Figure 34. Residual wavefront difference between the Hartmann measured wavefront and the theoretical wavefront.

By altering the Code V model with a upward lateral shift to the second prism of 0.7mm with a 2° rotation, we were able to get a wavefront change with roughly the same magnitude as seen in our Hartmann test as shown below in Figure 35. The general similarities between the wavefront changes shown in Figure 34 and Figure 35 indicates this decenter and rotation are likely the most significant manufacturing errors within our prism.

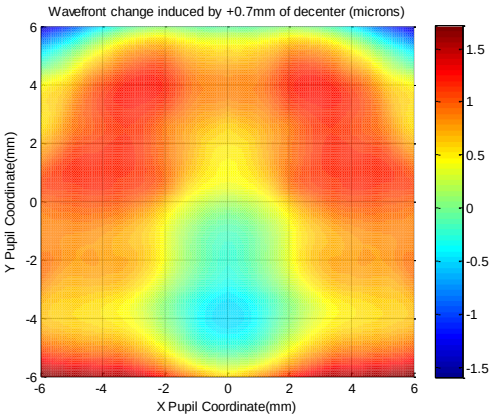

Figure 35. Wavefront change induced by 0.7mm of decenter and 2° of rotation to the second freeform wedge

The Hartmann test is also capable of showing us how our prism introduces wavefront distortion at off-center viewing angles. This is useful because it simulates the altered viewing experience as seen by a user when they wear the prism at the designed eye-relief and allows us to determine the overall power of the prism and how it changes with view angles. Figure 36 shows viewing angles of (12.5˚,0˚) and (-12.5˚,0˚) while Figure 37 shows viewing angles of (0˚,11˚), and (0˚,-11˚).

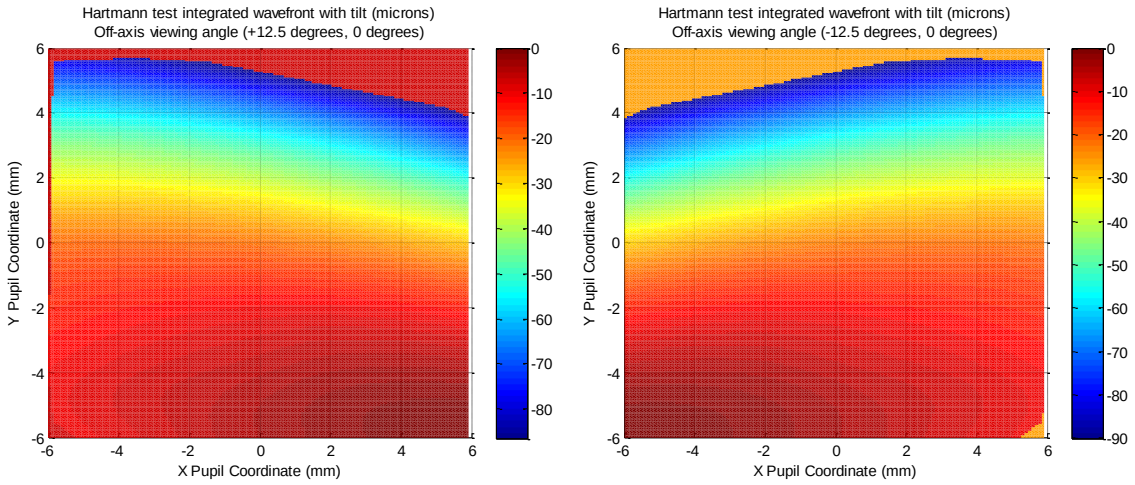

Figure 36. Shows the wavefront deviation introduced by the OST HMD prism at a view angle of (12.5˚,0˚) (left) (-12.5˚,0˚) and (right)

The wavefronts in Figure 36 should be roughly mirror images of each other as the prism is designed to be symmetrical about the Y-axis. Slight misalignments in the testing setup and prism itself cause this small discrepancy.

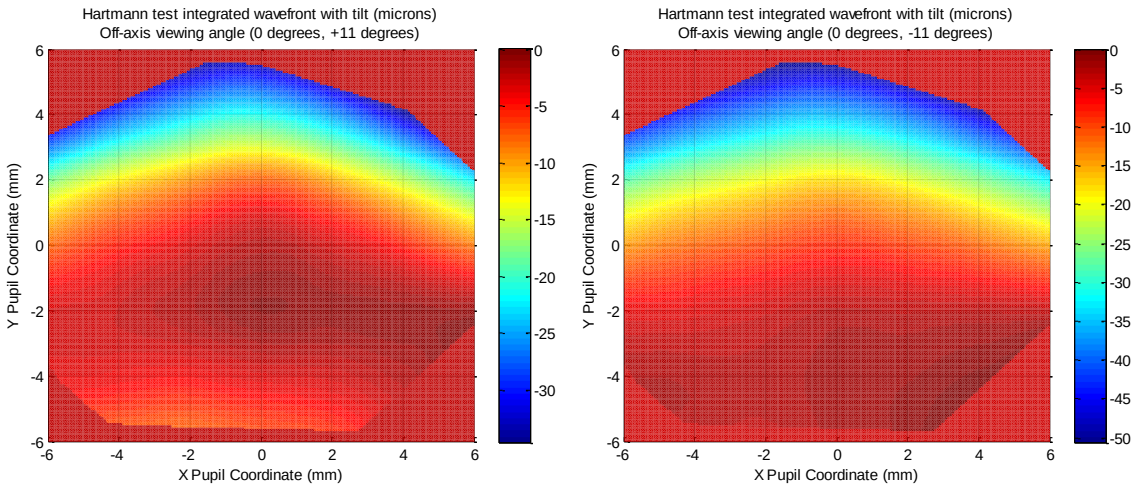

Figure 37. Shows the wavefront deviation introduced by the OST HMD prism at a view angle of (0˚,11˚) (left) and (0˚,-11˚) (right)

At these obscure view angles, the prism introduces large amounts of tilt to the wavefront. We removed the tilt to better show the residual power introduced by the freeform prism, the resulting wavefronts are shown below in Figure 38 and Figure 39.

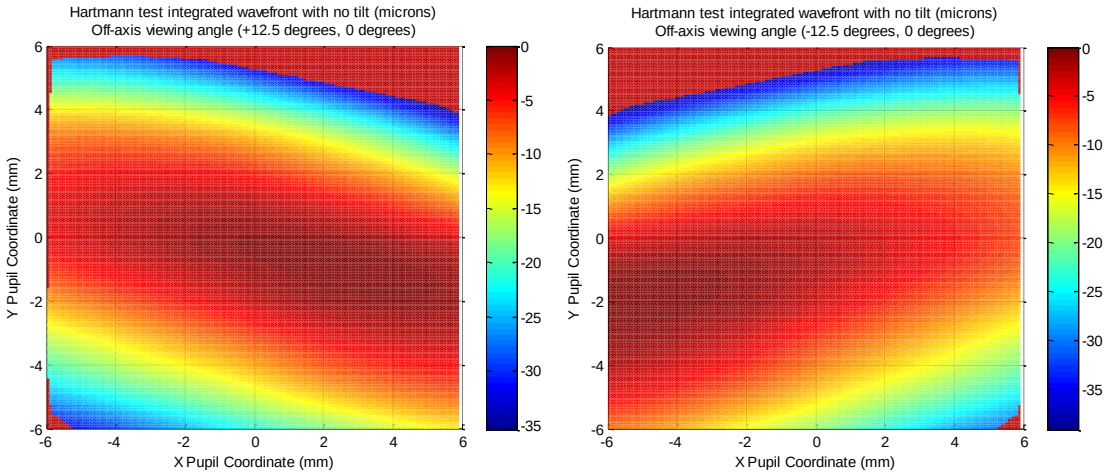

Figure 38. Shows the wavefront deviation without tilt at a view angle of (12.5˚,0˚) (left) and (-12.5˚,0˚) (right)

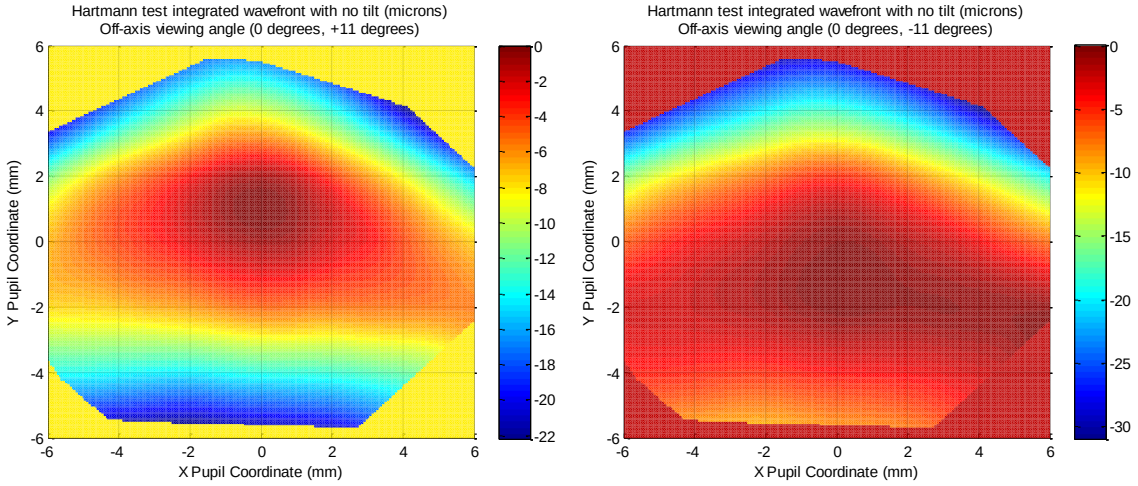

Figure 39. Shows the wavefront deviation without tilt at a view angle of (0˚,11˚) (left) and (0˚,-11˚) (right)

5. Conclusion

The ray trace method has shown to be accurate in determining both the monocular and binocular depth distortion in thick optical elements. We summarized how different setup parameters can be expected to alter the perceived depth of an object when viewed through a plane parallel plate. Then we used the same ray trace method to simulate the

depth distortion introduced by a well-corrected OST HMD prism. The results showed the freeform prism introduces more depth distortion and large amounts of astigmatism when compared to a PPP of similar thickness resulting from the residual power introduced by the prism.

In this paper we demonstrated how a Hartmann test is a simple low-cost solution to characterizing the wavefront deviation introduced by an OST HMD freeform prism. We showed that the primary source of measurement error, the centroiding error, can be drastically reduced by simultaneously using a scanning mask approach along with an extended viewing distance without the need for high-cost lenslet arrays. The sub-wavelength accuracy of this test is comparable to interferometric methods while being more versatile in that it can measure more highly sloped wavefronts. When testing a freeform prism, we were able to compare the results to the theoretical wavefronts produced with ray tracing software to estimate the decenter and tilt present in our prototype. Testing of the freeform prism at different viewing angles with the rotation axis centered at the pupil location provides insight in how the OST prisms will distort the view of a real world user.

References and Links

1. Rui Zhang and Hong Hua, "Design of a polarized head-mounted projection display using ferroelectric liquid-crystal-on-silicon microdisplays," Appl. Opt. 47, 2888-2896 (2008)
2. http://www.google.com/glass/start/
3. www.epson.com/moverio
4. http://lumus-optical.com/
5. http://www.sony.net/SonyInfo/News/Press/201502/15-016E/
6. Sangyoon Lee, Xinda Hu, Hong Hua, "Effects of Optical Combiner and IPD Change for Convergence on Near-Field Depth Perception in an Optical See-Through HMD", IEEE Transactions on Visualization & Computer Graphics, , no. 1, pp. 1, PrePrints PrePrints, doi:10.1109/TVCG.2015.2440272
7. Dewen Cheng, Yongtian Wang, Hong Hua, and M. M. Talha, "Design of an optical see-through head-mounted display with a low f-number and large field of view using a freeform prism," Appl. Opt. 48, 2655-2668 (2009)
8. F. Kellner, B. Bolte, G. Bruder, U. Rautenberg, F. Steinicke, M. Lappe, and R. Koch. Geometric calibration of head-mounted displays and its effects on distance estimation. *IEEE Transactions on Visualization and Computer Graphics*, 18(4):589-596, April 2012
9. E. Krujiff, J.E. Swan II, and S. Feiner. Perceptual issues in augmented reality revisited. In *Proc. 9th Int. Symp. Mixed and Augmented Reality*, pp. 3-12, 2010.

10. S.A. Kuhl, W.B. Thompson, and S.H. Creem-Regehr. HMD calibration and its effects on distance judgments. ACM Transactions on Applied Perception, 6(3):article 19, August 2009.
11. Y. Itoh and G. Klinker. Light-field correction for spatial calibration of optical see-through head-mounted displays. IEEE Transactions on Visualization and Computer Graphics, 21(4):471-480, April 2015.
12. D.M. Hoffman, A.R. Girshick, K. Akeley, and M.S. Banks. Vergence-accommodation conflicts hinder visual performance and cause visual fatigue. Journal of Vision, 8(3):33, 1-30, March 2008.
13. Stephan Stuerwald, "Error compensation in computer generated hologram-based form testing of aspheres," Appl. Opt. 53, 8249-8255 (2014)
14. Elena Stoykova, Georgi Minchev, and Ventseslav Sainov, "Fringe projection with a sinusoidal phase grating," Appl. Opt. 48, 4774-4784 (2009)
15. Hongwei Zhang, Shujian Han, Shugui Liu, Shaohui Li, Lishuan Ji, and Xiaojie Zhang, "3D shape reconstruction of large specular surface," Appl. Opt.51, 7616-7625 (2012)
16. Rafael Navarro and Esther Moreno-Barriuso, "Laser ray-tracing method for optical testing," Opt. Lett. 24, 951-953 (1999)
17. Dan Liu, Huijie Huang, Bingqiang Ren, Aijun Zeng, Yan Yan, and Xiangzhao Wang, "Scanning Hartmann test method and its application to lens aberration measurement," Chin. Opt. Lett. 4, 725-728 (2006)
18. http://www.optics.arizona.edu/sites/optics.arizona.edu/files/pdf/Historical-Development-Shack-Hartman-Wavefront-Sensor.pdf

19. http://www.vision.caltech.edu/bouguetj/calib_doc/

20. Hong Hua ; Xinda Hu ; Chunyu Gao ; Xiao Qin; Eyetracked optical see-through head-mounted display as an AAC device. Proc. SPIE 9117, Three-Dimensional Imaging, Visualization, and Display 2014, 91170T (June 5, 2014); doi:10.1117/12.2050843.

21. Wong, B. P. Woods, R. L. Peli, E. (2002). Stereoacuity at distance and near. *Optometry and Vision Science*, 79, 771–778.